AGU PUBLICATIONS

Geophysical Research Letters

RESEARCH LETTER
10.1002/2017GL075301

Key Points:
- Local seismic and geodetic data suggest that the Kaikōura earthquake involved little (if any) contribution of the subduction interface
- Overall rupture of the Kaikōura earthquake was slow (rupture velocity slower than 2 km/s)
- The Kekerengu fault is the major source of moment release. It appears to have ruptured at least twice, 11 s apart

Supporting Information:
- Supporting Information S1
- Table S1
- Table S2

Correspondence to:
C. Holden,
c.holden@gns.cri.nz

Citation:
Holden, C., Kaneko, Y., D'Anastasio, E., Benites, R., Fry, B. & Hamling, I. J. (2017). The 2016 Kaikōura earthquake revealed by kinematic source inversion and seismic wavefield simulations: Slow rupture propagation on a geometrically complex crustal fault network. *Geophysical Research Letters*, *44*. https://doi.org/10.1002/2017GL075301

Received 14 AUG 2017
Accepted 20 OCT 2017
Accepted article online 23 OCT 2017

The 2016 Kaikōura Earthquake Revealed by Kinematic Source Inversion and Seismic Wavefield Simulations: Slow Rupture Propagation on a Geometrically Complex Crustal Fault Network

C. Holden[1], Y. Kaneko[1], E. D'Anastasio[1], R. Benites[1], B. Fry[1], and I. J. Hamling[1]

[1]GNS Science, Lower Hutt, New Zealand

Abstract The 2016 Kaikōura (New Zealand) earthquake generated large ground motions and resulted in multiple onshore and offshore fault ruptures, a profusion of triggered landslides, and a regional tsunami. Here we examine the rupture evolution using two kinematic modeling techniques based on analysis of local strong-motion and high-rate GPS data. Our kinematic models capture a complex pattern of slowly ($V_r < 2$ km/s) propagating rupture from south to north, with over half of the moment release occurring in the northern source region, mostly on the Kekerengu fault, 60 s after the origin time. Both models indicate rupture reactivation on the Kekerengu fault with the time separation of ~11 s between the start of the original failure and start of the subsequent one. We further conclude that most near-source waveforms can be explained by slip on the crustal faults, with little (<8%) or no contribution from the subduction interface.

1. Introduction

The 2016 Kaikōura, New Zealand, earthquake struck the east coast of the northern South Island on 13 November 11:02 (universal time meridian). The damaging earthquake generated large (>10 m) fault displacements, widespread strong ground motion, and a regional tsunami (Hamling et al., 2017; Kaiser et al., 2017), triggered over 100,000 landslides in the epicentral region (Dellow et al., 2017) and large-scale (>15,000 km^2) slow slip events on the Hikurangi subduction interface (Wallace et al., 2017) and tremor and widespread seismic activation over much of the North Island (Wallace et al., 2017). The Kaikōura earthquake occurred in a complex tectonic region that marks the transition from the Hikurangi subduction zone to the north and the transpressional Alpine fault-dominated continental transform in central South Island. As such, examining rupture evolution during the Kaikōura earthquake is important and useful for understanding the nature of earthquake faulting processes in a tectonic transition characterized by a geometrically complex fault network.

In this study, we investigate the rupture process and slip history during the Kaikōura earthquake using local strong-motion and high-rate GPS waveforms and two complementary kinematic source modeling approaches based on spectral element method and discrete wave number method. The first approach performs numerical forward simulation of the seismic wavefield and iteratively fitting the simulated waveforms to the observed ones. The second is a finite fault slip inversion commonly used to infer the slip history of large earthquakes (e.g., Di Carli et al., 2010). In the first approach, numerical wavefield simulation accounts for a local 3-D velocity model including anelastic attenuation. However, it is computationally expensive and thus cannot be used to invert ground motions for a wide range of source parameter space. Conversely, finite fault inversion requires several simplifying assumptions about the source and seismic velocity structure but its low computational cost enables exploration of a wide range of source parameters. Since geodetically derived slip models of the Kaikōura earthquake indicate a large degree of complexity of the ruptured fault system (Clark et al., 2017; Hamling et al., 2017), rupture-time histories inferred from either technique are nonunique; hence, robust features are better identified from mutual features present in the results of both approaches.

2. Kinematic Slip History Inferred From Forward Wavefield Simulations

2.1. Simulation Method

To explain dominant signals in the local waveform data, we compute synthetic seismograms using open source seismic wave propagation software SPECFEM3D (Komatitsch & Tromp, 1999; Komatitsch & Vilotte,

1998). Our approach utilizes 3-D velocity and attenuation models for New Zealand (Eberhart-Phillips & Bannister, 2015; Eberhart-Phillips et al., 2010) and topography and bathymetry of the region. We use a finite fault approach (e.g., Hjörleifsdóttir et al., 2009) where a set of point sources are used to represent the spatiotemporal evolution of slip on the faults ruptured during the Kaikōura earthquake. To reduce the degree of unknowns, we use an a priori fault slip model (Clark et al., 2017) as a constraint for the fault geometry and the final slip distribution and only vary the rupture initiation times of major fault segments and rise time distribution, with the local rise time being proportional to the square root of slip (e.g., Aagaard & Heaton, 2008; Graves & Pitarka, 2010) (Figure 1a). In this slip model, there are a total of 21 planar fault segments with their dip constrained by geologically estimated values (Hamling et al., 2017). The Hikurangi subduction interface at the base of crustal faults is included, although the relatively small slip (up to 2 m) does not contribute much (~8%) to the overall moment (Figure 1a). The Papatea fault (Figure 1) which resulted in large (up to ~10 m) surface offsets extending up to ~13 km in length (Hamling et al., 2017) is not included in our model as elastic dislocation models fail to explain the observed asymmetrical and distributed deformation around the fault (Hamling et al., 2017). The detail of the model setup is described in section S1 in the supporting information.

2.2. Rupture Time Histories and Waveform Fits

After simulating 65 source models with different source half durations and distributions of rupture initiation times and rupture velocity as detailed in section S1, we determine our preferred model that leads to the smallest waveform misfit and can explain dominant phases in near-field velocity waveforms (see details in section S1). We compare our results to three-component velocity waveform data from a total of 17 regional stations composed of 14 strong motion stations and 3 high-rate GPS sites from the New Zealand GeoNet network (Figure 1). The acceleration waveforms are integrated into velocity and filtered using a Butterworth band-pass filter from 0.01 to 0.3333 Hz (a period band of 3 to 100 s). The upper frequency limit is chosen to eliminate the complexity in high-frequency waveforms arising from small-scale complexities in actual 3-D velocity structure that are not captured by the present velocity model. The GPS velocity waveforms are derived from the time derivative of displacement waveforms, which are then band-pass filtered at the same frequency range. Due to instrumental glitches, the timing of seismic station MGCS (Figure 1) is manually corrected.

The preferred model indicates that the rupture began on the Humps fault and propagated predominately toward the northeast at a rupture velocity of ~1.9 km/s on the "Humps-Hundalee fault system" (Figure 2a). The rupture moves onto the offshore, Point Kean fault at 31 s after the origin time, and then continues onto the northern faults including Upper Kowhai, Kekerengu, and Needles at a velocity of ~2.0 km/s (Figure 2a). Interestingly, we find that dominant phases in observed velocity seismograms in the northern stations cannot be explained by continuous propagation of a single rupture from the southwest to northeast (Figure S2). At several stations (e.g., KEKS and WDFS), two dominant phases separated by ~11 s are visible (Figure S2), indicating rupture reactivation on parts of the Kekerengu fault, where the maximum slip at the ground surface was ~12 m (Stirling et al. 2017) and a total slip of ~20 m was inferred from the geodetically derived slip model. In the preferred model, we partition the total slip on the Kekerengu and Needles faults derived from Clark et al. (2017) into two rupture episodes, with the first and second ruptures accounting for ~60% and ~40% of the total slip in the upper 10 km, respectively (Figure S1). The rupture initiation time and rupture velocity are different for these two rupture episodes. The first rupture on the upper 10 km of the Kekerengu fault began to propagate at 48 s after the origin time (Figure S1). At 11 s later, the second rupture nucleated at about 10 km depth and broke the largest asperity with ~20 m of slip on the same fault (Figure S1). The propagation velocity of the first rupture is ~2.0 km/s, while that of the second rupture is quite slow (~1.5 km/s) (Figure S1). Such source model can fit two dominant phases separated by ~11 s in near-fault waveforms (Figure 3a).

In our preferred model, we assume that the rupture of the subduction interface occurs following the rupture of the largest asperity on the Kekerengu fault (Figure 2a); however, the rupture timing of the subduction interface is not well constrained in this model as the relatively small contribution of the interface to the overall moment makes it difficult to resolve the timing of the rupture (Figure S3). The overall duration of the entire rupture is about 90 s, with the largest seismic moment release occurring at 60–80 s after the origin time (Figures 2a and 2b).

Observed and synthetic velocity waveforms are compared in Figures 3a, S4, and S5, which show a good overall agreement. Onset, amplitude, and polarities of dominant phases are well matched for three

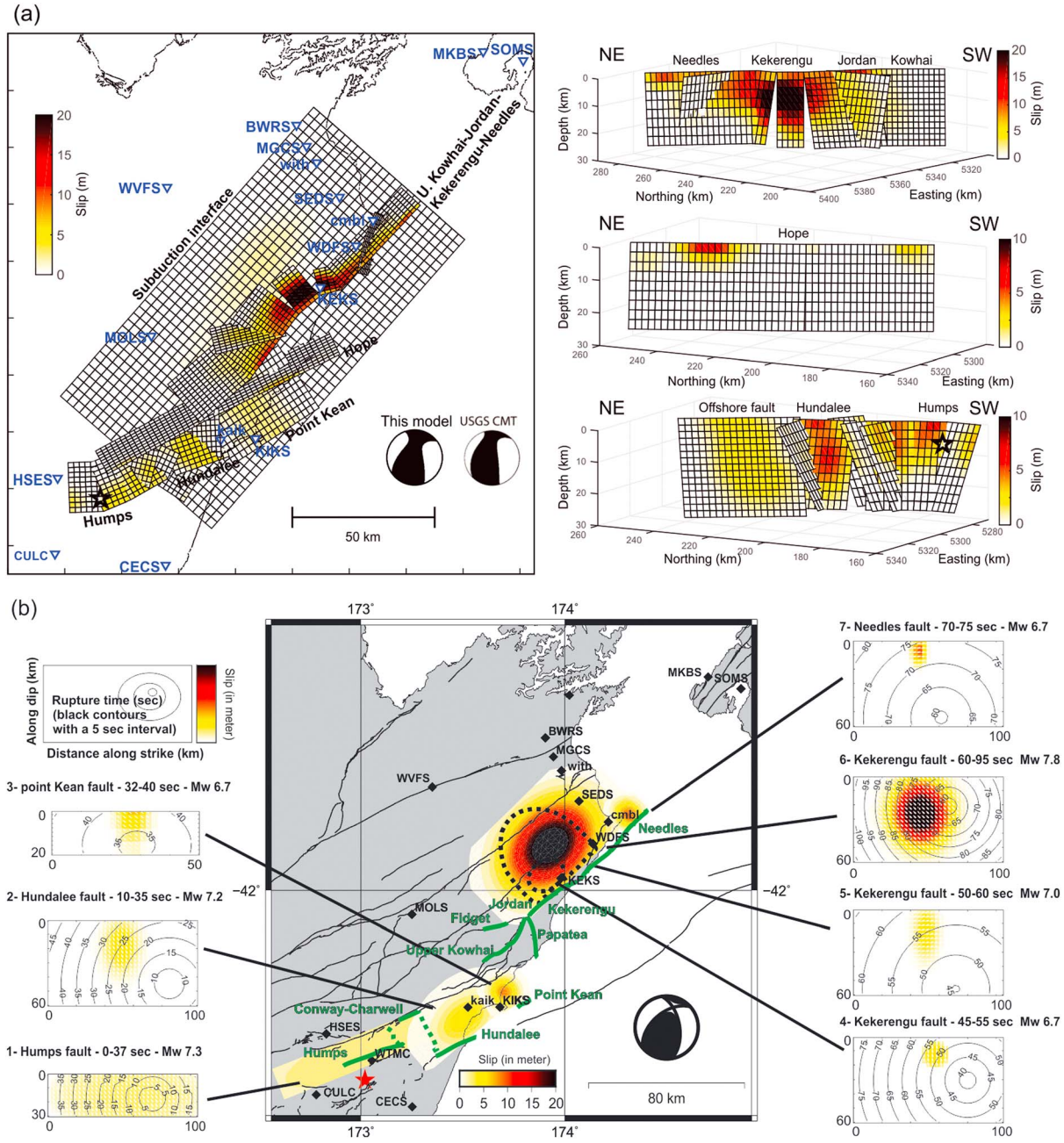

Figure 1. Slip models of the Kaikōura earthquake (a) obtained by Clark et al. (2017) and (b) inferred from kinematic source inversion in this study. The locations of strong-motion and high-rate GPS stations used in this study are indicated. Overall moment tensors are indicated. Mapped fault traces (black lines) are extracted from NZ active faults database (Langridge et al., 2016) and Kaikōura earthquake surface ruptures (green lines) interpreted from Stirling et al. (2017).

components. For northern stations, the synthetic waveforms match particularly well with the largest phases in the north-south and vertical components (section S3). Waveform misfits for the north-south component are larger because the observed amplitudes are larger. For southern stations, the preferred model reproduces dominant amplitudes and phases well for all components in near-fault stations (e.g., KIKS and kaik). However, with our model, complex, multiple peaks in the first ~50 s at other southern stations (e.g., CECS, CUCL, and HSES) are not captured by the synthetic seismograms. Overall agreement between synthetic and observed waveforms supports previous findings (Clark et al., 2017) that many crustal faults were ruptured during the Kaikōura earthquake, while there was little (~8%) contribution from slip on the subduction interface to the overall moment.

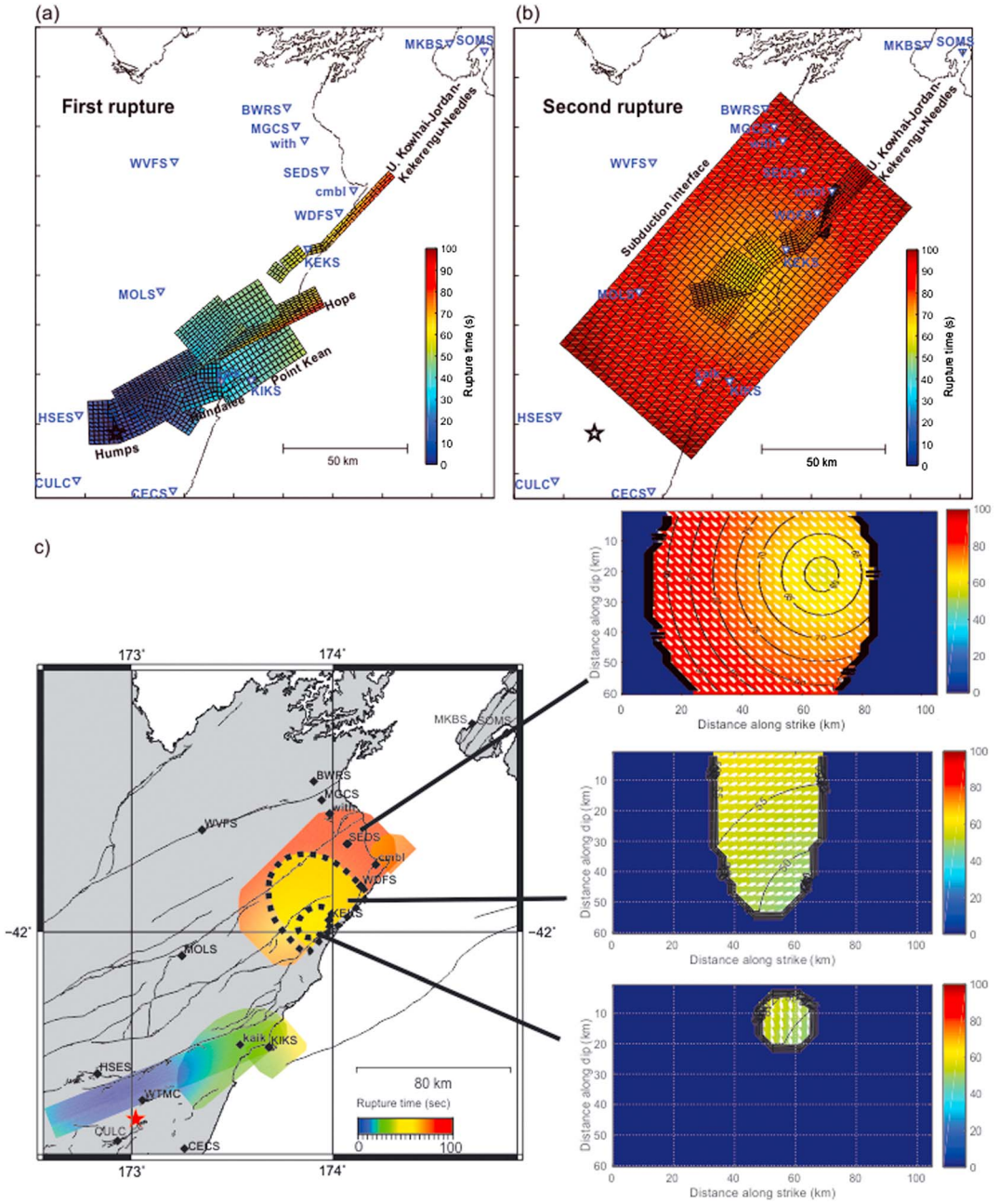

Figure 2. Rupture initiation times on the faults inferred from (a, b) forward wavefield simulations and (c) kinematic source inversion. Mapped fault traces (black lines) are extracted from NZ active faults database (Langridge et al., 2016).

3. Kinematic Slip History Inferred From Finite Fault Slip Inversion

3.1. Data Set, Fault Geometry, and Inversion Method

We invert kinematic rupture parameters for a wide range of fault planes, including the subduction interface. We found that ground motion modeling for five crustal fault planes provided significant improvement to the misfit to the recorded data: Humps, Hundalee, point Kean, Kekerengu, and Needles. Fault plane locations are imposed by best fit solutions from the inversion of GPS and interferometric synthetic aperture radar (InSAR) data (Hamling et al., 2017), geological surface rupture observations (Stirling et al., 2017), and geophysical marine data acquired soon after the earthquake (Clark et al., 2017). We invert for an elliptical distribution of slip on each fixed-geometry fault plane (Di Carli et al., 2010). The detail of the inversion parameters is described in

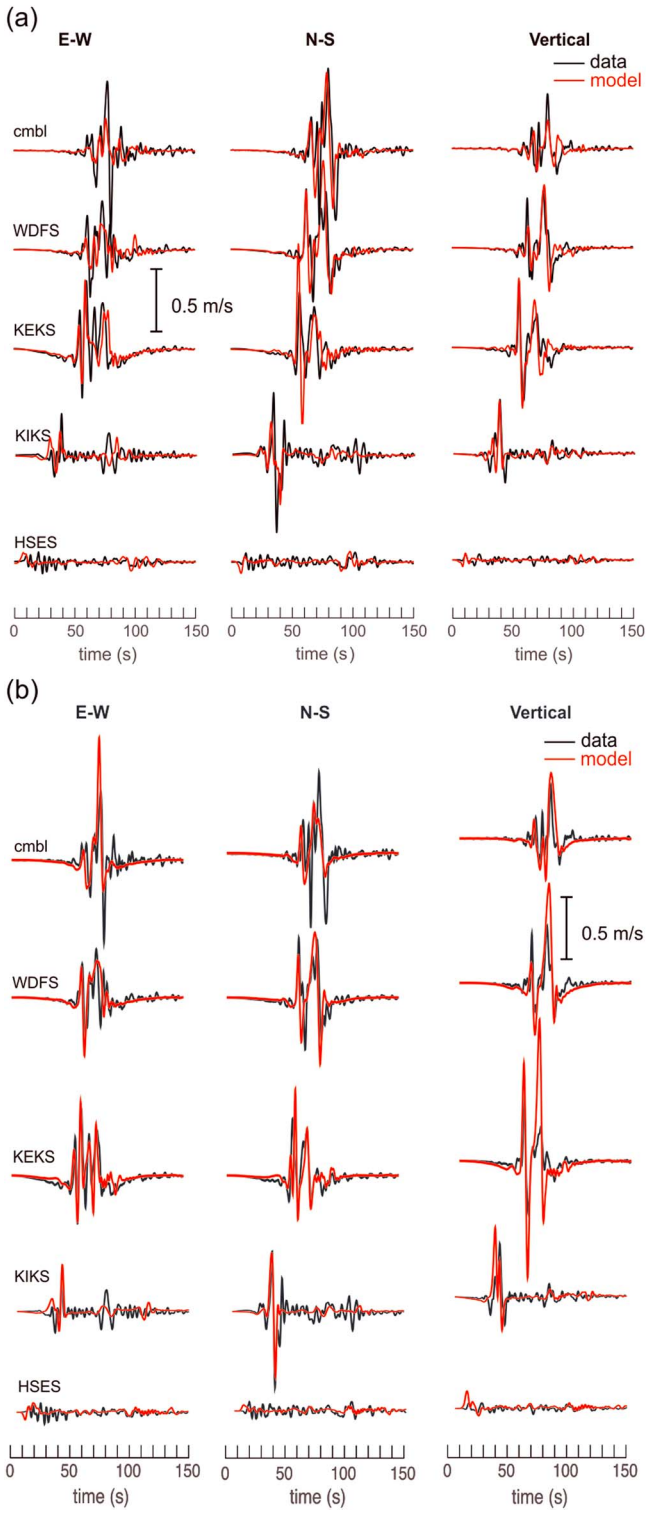

Figure 3. Observed (black line) and synthetic (red line) velocity seismograms band-pass filtered between 3 and 100 s at five selected near-field stations for the preferred models derived from (a) forward wavefield simulation and (b) kinematic source inversion. Station names with captial letters correspond to strong-motion stations, whereas those with lowercase letters correspond to high-rate GPS stations.

section S2. Synthetic seismograms are computed with the discrete wavenumber approach of Bouchon (1981), using a regional 1-D velocity model from Eberhart-Phillips and Bannister (2015). To search for a minimum waveform misfit, we use the nonlinear Neighborhood Algorithm (Sambridge, 1999). The misfit function is a least squares scheme applied to 150 s of the three components of recorded ground motion for each station beginning at the earthquake origin time at each station.

3.2. Rupture Time Histories and Waveform Fits

Results suggest that the rupture propagated on multiple segments, mostly continuously and in a northeastward direction (Figures 1b and 2b). To the south, the first 50 s of the rupture occur from the epicenter up to point Kean fault, offshore Kaikōura. The central Fidget-Jordan segments are not included in this model as these do not contribute much to the recorded ground motions. However, they exhibit significant coseismic slip (Hamling et al., 2017) and undeniably participated to the rupture sequence. The rupture then continues north of Kaikōura to Cape Campbell from 45 to 75 s. South of Kaikōura, the first segment initiates near the epicenter and ruptures part of the "Humps fault system" along a 100 km long fault, from 0 to 37 s. The second segment "Hundalee fault" ruptured from 14 to 35 s. The third segment, point Kean fault, offshore Kaikōura, ruptured from 32 to 40 s. North of Kaikōura, the fourth segment, "Kekerengu fault" ruptured in three successive asperities from south near KEKS to north. Inversions were run with three different waveform time constraints to isolate the various contributions from different parts of the Kekerengu fault plane. The three slip patches are rupturing as follows: (1) from 47 to 57 s, equivalent to a M_w6.7 earthquake; (2) from 49 to 60 s (a fast rupture of 4 km/s), equivalent to a M_w7.0 earthquake; and (3) from 57 to 95 s (a very slow rupture of 1.5 km/s), equivalent to a M_w7.8 earthquake (contributing to 65% of total moment release).

Finally, the last segment offshore to the north, "Needles," ruptures from 69 to 76 s. The source slip model is characterized by five main segments: Humps, Hundalee, point Kean, Kekerengu, and Needles with Humps/Hundalee/Kekerengu (third rupture) contributing to 88% of the total moment release. The total moment is equivalent to a M_w7.9 earthquake, consistent with the model described in section 2.

The waveform fit is overall very good at all near-source stations (Figures 3b, S6, and S7). Onset, amplitude, and polarity criteria are well matched for all three components. For stations to the north, where most of the energy release occurs, the model fits the largest amplitudes of the horizontal components well. The vertical component is slightly overpredicted at these sites, except for KEKS where the discrepancy is large. Kinematic solutions are highly nonunique. Proximity to the source will exaggerate slight discrepancies between models. In this study, the model described in section 2 produces "better" vertical motions at KEKS than this model. For stations to the south of the rupture, we reproduce the dominant phases, including amplitudes, particularly well and for all components However, with our simple fault and velocity model we are not able to capture the rupture details from the multiple small southern fault planes that are causing the long-duration low-amplitude and high-frequency signal. This is particularly true for the three closest stations to the epicenter, HSES, CECS, and CULC.

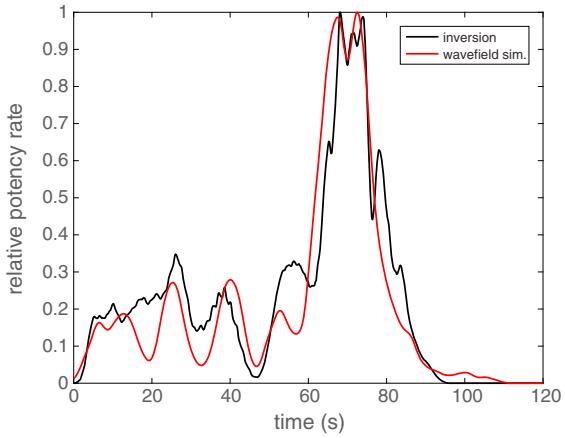

Figure 4. Estimated source time functions for the Kaikōura earthquake using forward wavefield simulation (Model A) and kinematic source inversion (Model B). Both models result in M_w7.9.

4. Discussion

4.1. General Characteristics

Rupture models obtained from the different waveform analysis techniques share key common characteristics. We highlight these common characteristics and suggest that they are robust features of the rupture sequence. In what follows, we refer to the preferred source model obtained from forward wavefield simulation as Model A and that of kinematic inversion as Model B. Both Models A and B show multiple fault ruptures extending over 150 km and lasting for ~90 s. Among the faults ruptured during the earthquake, the largest asperity is located on the Kekerengu fault, with up to ~20 m of slip. This is compatible with other observations based on geologic and geodetic observations of surface deformation. Despite the large slip, the corresponding rupture velocity is surprisingly slow (~1.5 km/s) in both models. In fact, rupture velocities for most fault segments are less than ~2.0 km/s (Figures 2a and 2b), which are slower than the average rupture velocity of most crustal earthquakes (Somerville et al., 1999). The slow rupture velocities could be associated with rupturing of multiple immature faults and extensive on- and off-fault inelastic deformation that led to a large amount of energy dissipation, as hinted from the analysis of near-fault seismic waveforms (Kaneko et al., 2017). Both Models A and B show excellent agreement in rupture initiation times and durations of the main fault planes (31 and 30 s for point Kean fault offshore Kaikōura fault and 59 and 60 s for the main Kekerengu asperity for Models A and B, respectively). Agreement for both models in major rupture durations and related onset times is particularly well illustrated in the source-time function plot shown in Figure 4. An important conclusion from both models is how the rupture exclusively propagated to the north of the epicenter despite increased stress to the south from the recent 2010–2011 Canterbury earthquake sequence (Kaiser et al., 2016) occurring less than 100 km south of the Kaikōura epicenter. Interestingly, slow rupture velocities, rupture directivity, and source-time functions are very similar to those by Cesca et al. (2017) and Hollingsworth et al. (2017) using different data set and inversion approaches. The rupture also seems to have bypassed the Hope fault even though it is the source of the largest seismic hazard in the region (Stirling et al., 2012). Neither Model A nor B requires significant slip on the subduction interface or the Papatea fault. These are discussed in more details in the following sections.

While both models demonstrate that most of nearfield velocity waveforms (in the period of 3–100 s) can be explained by slip on the crustal faults, the subduction interface is included in Model A, whereas Model B is able to explain most waveforms without any interface contribution. Further discussion is included in section 4.3. There are other fault segments that are known to have ruptured with possibly up to several meters of slip that are not included in Model B. Due to the sparse station distribution around the Jordan Thrust and Upper Kowhai fault rupture area, the Jordan Thrust and Upper Kowhai faults are not clearly captured by local seismic data. While the source models based on synthetic aperture radar (SAR) and lidar data and field observations (Clark et al., 2017; Hamling et al., 2017) show rupture of the Jordan Thrust and Upper Kowhai fault segments either coseismically or postseismically and were therefore included in Model A, they are poorly sampled by local seismic waveforms and hence excluded in Model B.

4.2. Rupture Reactivation on the Kekerengu Fault

Both Models A and B show multiple fault ruptures extending over 150 km and lasting for ~90 s, with continuous rupture along each separate fault plane apart from the rupture reactivation on the Kekerengu-Needles faults (Figure 2). Model A suggests that the second and main asperity overlaps the first one by 40%; Model B suggests that the second and main asperity totally overlaps the first one. Rerupturing of major asperities (or rupture reactivation) has been previously inferred for the 2011 *M*9.0 Tohoku-Oki earthquake from a kinematic source model (Lee et al., 2011) as well as a dynamic rupture model (Galvez et al., 2016). Several mechanisms have been proposed to explain rupture reactivation including rupture in a heterogeneous distribution of prestress (Goto et al., 2012) and thermally activated slip weakening with two sequential strength drops (Galvez et al., 2016; Kanamori & Heaton, 2000). Unlike the Tohoku-Oki earthquake, rupture

reactivation in the Kaikōura earthquake only involved a portion of the Kekerengu fault (Figures 1b and S1). At the same time, the availability of near-fault (<10 km) waveforms at stations KEKS and WDFS may provide robust evidence of possible rupture overlap with significant (greater than several meters) slip on the Kekerengu fault (Figures 3a and 3b). We speculate that the initiation of the delayed rupture of the main asperity may have been caused by a gradual decrease in the fault dip angle with depth, where the Kekerengu fault is expected to be listric and joins the subduction interface at ~25 km depth (Figure S8). Such fault geometry, implying different levels of prestress at different depths, may have led to the delayed onset of the asperity rupture at depth and subsequent reactivation of rupture on parts of the Kekerengu fault. This hypothesis and others can be tested with future dynamic rupture modeling.

4.3. Possible Contribution From Subduction Interface Rupture

Earthquake hypocenter locations and tomographic models suggest the existence of a subduction interface in the Kaikōura source region (Williams et al., 2013). However, whether the subduction interface is seismically active has been widely debated (Reyners et al., 2017) and carries direct implication for New Zealand seismic hazard (Stirling et al., 2012). Various observations made after the Kaikōura earthquake provide some evidence for rupture of the subduction interface. Tsunami wave heights of up to ~7 m are not fully explained by a purely crustal offshore fault source (Hamling et al., 2017). A large triggered slow slip at depth below the northern crustal faults presents the characteristics of a subduction rupture (Wallace et al., 2017). Detailed aftershock relocation also indicates rupturing on a shallow dipping large fault plane. Recent source models based on teleseismic and/or regional data suggest that the interface did contribute to the overall rupture (Bai et al., 2017; Duputel & Rivera, 2017). The suggestion of subduction interface involvement is compatible with backprojection results (Kaiser et al., 2017), which illuminate deep (20–30 km) radiation beneath the Kekerengu fault at about 60 s contemporaneous to large moment release between 60 and 80 s. Finally, this earthquake presents similar characteristics in terms of maximum surface slip, magnitude, and tectonic setting to the *M*8.2 1855 Wairarapa earthquake, which most likely involved a large component of the subduction interface (Beavan & Darby, 2005; Rodgers & Little, 2006).

However, many observations strongly support evidence of minor (if any) contribution of the interface in the overall rupture. Our results show that near-field waveforms in a wide range of periods (3–100 s) can be mostly explained with crustal fault rupture only as shown in both Models A and B. Additional tests indicate that the subduction interface slip constrained by geodetic observations (Clark et al., 2017) is unresolvable by the near-field strong-motion waveforms (Figure S3). Although some phases in the near-field waveforms could be fit by source models allowing larger slip (~8 m) on the subduction interface, such models significantly overpredict geodetic data and hence would be unrealistic (Figure S3). The fault geometry inferred from field observations (Stirling et al., 2017) indicates that major slip on large and low angle faults, which was previously interpreted as slip on the interface (Duputel & Rivera, 2017), is likely splay faults rather than the subduction interface. Geodetic forward modeling of Bai et al. (2017), which suggests that the interface did contribute to the overall rupture, does not agree well with polarities and amplitudes measured at most GPS sites (Figure S9). Coastal uplift data (Clark et al., 2017) support a minimal contribution (<10%) of the interface. Cesca et al. (2017) model regional and teleseismic seismograms, GPS, and InSAR data without involving a rupture on the plate interface. Finally, Kaikōura earthquake aftershocks show a mixture of strike slip and oblique reverse faulting mechanisms and hence are not representative of large subduction interface rupture (Kaiser et al., 2017).

4.4. Possible Contribution From Papatea Fault Rupture

Neither of our source models involve rupture of the Papatea fault even though large (up to ~10 m) surface offsets extending up to ~13 km in length were identified in the field and estimated from SAR azimuth and range offsets (Hamling et al., 2017). We attempt to isolate the contribution of rupture of the Papatea fault to local displacement waveforms by forward modeling a range of scenarios for the Papatea fault rupture. While not all of the possible parameter space is explored, we find a relatively minor contribution of the Papatea fault rupture to local waveforms despite its large slip. The main reason is that there are no nearby strong-motion or high-rate GPS stations around the Papatea fault. The closest one is seismic station KEKS located ~22 km away from the Papatea fault; the same station is only 2.7 km away from the Kekerengu fault. Because of this, the contribution from the shorter (~13 km) Papatea fault is contaminated by much larger contribution from the rupture of the closer and larger (30–40 km long) asperity spanning the Kekerengu, Needles, and possibly Jordan Thrust faults. This makes it difficult to isolate the signals from the Papatea fault

rupture in local waveforms. In addition, classical elastic dislocation models fail to explain asymmetrical and distributed deformation around the Papatea fault (Hamling et al., 2017), indicating that any source models that do not account for the complex deformation might not be a proper representation of the rupture on the Papatea fault. Future effort is directed toward a source model that can reconcile geological and geophysical observations.

5. Conclusions

Our study shows that most of nearfield waveforms (in the period of 3–100 s) can be explained by slip on the crustal faults, with little ($<$ 8%) or no contribution from slip on the subduction interface. Interestingly, the rupture excluded the Hope fault and propagated from south to north despite the region south of the epicenter being stressed by the recent Canterbury earthquakes. Our slip models indicate possible rerupturing of parts of the Kekerengu fault; the delayed rupture nucleated ~11 s later and broke a major asperity with ~20 m of slip. Modeled slow average rupture velocities can be attributed to the fact that the earthquake broke many relatively young and immature faults, during which the large amount of available energy may have been dissipated as inelastic deformation. More analysis is required to understand what controls the slow rupture velocities.

Acknowledgments

We thank Carl Tape for providing us the computational mesh for forward wavefield simulations. We also thank Ronni Grapenthin (New Mexico Tech) for pointing out a missing time interval in high-rate GPS data. We are grateful to Emily Warren-Smith and the two reviewers for prompt and beneficial reviews of this article. We also wish to acknowledge the contribution of the New Zealand eScience Infrastructure (NeSI) high-performance computing facilities to the results of this research. NZ's national facilities are provided by NeSI and funded jointly by NeSI's collaborator institutions and through the Ministry of Business, Innovation, and Employment Research Infrastructure programme. This work was supported by a combination of public funding from the Government of New Zealand and Marsden fund. The strong-motion data and high-rate GPS data used in this study are publically available and can be downloaded from New Zealand's GeoNet website (https://www.geonet.org.nz). Processed GPS time series are available upon request.

References

Aagaard, B. T., & Heaton, T. H. (2008). Constraining fault constitutive behavior with slip and stress heterogeneity. *Journal of Geophysical Research*, *113*, B04301. https://doi.org/10.1029/2006JB004793

Bai, Y., Lay, T., Cheung, K. F., & Ye, L. (2017). Two regions of seafloor deformation generated the tsunami for the 13 November 2016, Kaikōura, New Zealand earthquake. *Geophysical Research Letters*, *44*, 6597–6606. https://doi.org/10.1002/2017GL073717

Beavan, J., & Darby, D. (2005). Fault slip in the 1855 Wairarapa earthquake based on new and reassessed vertical motion observations: Did slip occur on the subduction interface?, The 1855 Wairarapa Earthquake Symposium — Proceedings volume published by greater wellington regional council greater wellington publication number: GW/RINV-T-05/205 ISBN: 0-909016-87-9 September 2005.

Bouchon, M. (1981). A simple method to calculate Green's functions for elastic layered media. *Bulletin of the Seismological Society of America*, *71*, 959–971.

Cesca, S., Zhang, Y., Mouslopoulou, V., Wang, R., Saul, J., Savage, M., … Dahm, T. (2017). Complex rupture process of the M_w 7.8, 2016, Kaikoura earthquake, New Zealand, and its aftershock sequence. *Earth and Planetary Science Letters*, *478*, 110–120. https://doi.org/10.1016/j.epsl.2017.08.024

Clark, K. J., Nissen, E. K., Howarth, J. D., Hamling, I. J., Mountjoy, J. J., Ries, W. F., … Strong, D. T. (2017). Highly variable coastal deformation in the 2016 M_w7.8 Kaikōura earthquake reflects rupture complexity along a transpressional plate boundary. *Earth and Planetary Science Letters*. https://doi.org/10.1016/j.epsl.2017.06.048

Dellow, S., Massey, C., Cox, S., Archibald, G., Begg, J., Bruce, Z., … Little, M. (2017). Landslides caused by the 14 November 2016 M_w7.8 Kaikōura earthquake and the immediate response. *Bulletin of the New Zealand Society for Earthquake Engineering*, *50*(2).

Di Carli, S., François-Holden, C., Peyrat, S., & Madariaga, R. (2010). Dynamic inversion of the 2000 Tottori earthquake based on elliptical subfault approximations. *Journal of Geophysical Research*, *115*, B12328. https://doi.org/10.1029/2009JB006358

Duputel, Z., & Rivera, L. (2017). Long-period analysis of the 2016 Kaikōura earthquake. *Physics of the Earth and Planetary Interiors*, *265*, 62–66. https://doi.org/10.1016/j.pepi.2017.02.004

Eberhart-Phillips, D., & Bannister, S. C. (2015). 3-D imaging of the northern Hikurangi subduction zone, New Zealand: Variations in subducted sediment, slab fluids and slow slip. *Geophysical Journal International*, *201*(2), 838–855. https://doi.org/10.1093/gji/ggv057

Eberhart-Phillips, D., McVerry, G. H., & Reyners, M. E. (2010). Influence of 3D distribution of Q and crustal structure on ground motions from the 2003 M_w 7.2 Fiordland, New Zealand, earthquake. *Bulletin of the Seismological Society of America*, *100*(3), 1225–1240. https://doi.org/10.1785/0120090148

Galvez, P., Dalguer, L. A., Ampuero, J. P., & Giardini, D. (2016). Slip reactivation during the 2011 M_w 9.0 Tohoku earthquake: Dynamic rupture and ground motion simulations. *Bulletin of the Seismological Society of America*, *106*(3), 819–831. https://doi.org/10.1785/0120150153

Goto, H., Yamamoto, Y., & Kita, S. (2012). Dynamic rupture simulation of the 2011 off the Pacific coast of Tohoku Earthquake: Multi-event generation within dozens of seconds. *Earth, Planets and Space*, *64*, 11. https://doi.org/10.5047/eps.2012.06.002

Graves, R. W., & Pitarka, A. (2010). Broadband ground-motion simulation using a hybrid approach. *Bulletin of the Seismological Society of America*, *100*, 2095–2123. https://doi.org/10.1785/0120100057

Hamling, I. J., Hreinsdóttir, S., Clark, K., Elliott, J., Liang, C., Fielding, E., … Stirling, M. (2017). Complex multifault rupture during the 2016 M_w 7.8 Kaikoura earthquake, New Zealand. *Science*, *356*, eaam7194. https://doi.org/10.1126/science.aam7194

Hjörleifsdóttir, V., Kanamori, H., & Tromp, J. (2009). Modeling 3-D wave propagation and finite slip for the 1998 Balleny Islands earthquake. *Journal of Geophysical Research*, *114*, B03301. https://doi.org/10.1029/2008JB005975

Hollingsworth, J., Ye, L., & Avouac, J.-P. (2017). Dynamically triggered slip on a splay fault in the M_w 7.8, 2016 Kaikoura (New Zealand) earthquake. *Geophysical Research Letters*, *44*, 3517–3525. https://doi.org/10.1002/2016GL072228

Kaiser, A. E., Balfour, N., Fry, B., Holden, C., Litchfield, N. J., Gerstenberger, M. C., … Gledhill, K. R. (2017). The 2016 Kaikōura, New Zealand, earthquake: Preliminary seismological report (2017). *Seismological Research Letters*, *88*(3), 1–13. https://doi.org/10.1785/0220170018

Kaiser, A. E., Holden, C., Hamling, I. J., Hreinsdottir, S., Horspool, N. A., Massey, C. I., … Wallace, S. (2016). The 2016 valentine's day M_w 5.7 Christchurch earthquake: Preliminary report, paper no. O-20 IN: Reducing risk raising resilience: New Zealand society for earthquake engineering technical conference. Christchurch: New Zealand Society for Earthquake Engineering. 1–3 April.

Kanamori, H., & Heaton, T. H. (2000). Microscopic and macroscopic physics of earthquakes. In J. B. Rundle, D. L. Turcotte, & W. Klein (Eds.), *Geocomplexity and the Physics of Earthquakes, Geophysical Monograph* (Vol. 120, pp. 147–164). Washington, DC: American Geophysical Union.

Kaneko, Y., Fukuyama, E., & Hamling, I. J. (2017). Slip-weakening distance and energy budget inferred from near-fault ground deformation during the 2016 M_w7.8 Kaikōura earthquake. *Geophysical Research Letters*, *44*, 4765–4773. https://doi.org/10.1002/2017GL073681

Komatitsch, D., & Tromp, J. (1999). Introduction to the spectral-element method for 3-D seismic wave propagation. *Geophysical Journal International*, *139*(3), 806–822. https://doi.org/10.1046/j.1365-246x.1999.00967.x

Komatitsch, D., & Vilotte, J. P. (1998). The spectral-element method: An efficient tool to simulate the seismic response of 2D and 3D geological structures. *Bulletin of the Seismological Society of America*, *88*(2), 368–392.

Langridge, R. M., Ries, W. F., Litchfield, N. J., Villamor, P., Van Dissen, R. J., Rattenbury, M. S., … Stirling, M. W. (2016). The New Zealand active faults database. *New Zealand Journal of Geology and Geophysics*, *59*(1), 86–96. https://doi.org/10.1080/00288306.2015.1112818

Lee, S.-J., Huang, B.-S., Ando, M., Chiu, H.-C., & Wang, J.-H. (2011). Evidence of large scale repeating slip during the 2011 Tohoku-Oki earthquake. *Geophysical Research Letters*, *38*, L19306. https://doi.org/10.1029/2011GL049580

Reyners, M., Eberhart-Phillips, D., & Bannister, S. (2017). Subducting an old subduction zone sideways provides insights into what controls plate coupling. *Earth and Planetary Science Letters*, *466*, 53–61. https://doi.org/10.1016/j.epsl.2017.03.004

Rodgers, D. W., & Little, T. A. (2006). World's largest coseismic strike-slip offset: The 1855 rupture of the Wairarapa Fault, New Zealand, and implications for displacement/length scaling of continental earthquakes. *Journal of Geophysical Research*, *111*, B12408. https://doi.org/10.1029/2005JB004065

Sambridge, M. (1999). Geophysical inversion with a neighbourhood algorithm—I. Searching a parameter space. *Geophysical Journal International*, *138*, 479–494. https://doi.org/10.1046/j.1365-246X.1999.00876.x

Somerville, P. G., Irikura, K., Graves, R., Sawada, S., Wald, D., Abrahamson, N., … Kowada, A. (1999). Characterizing earthquake slip models for the prediction of strong ground motion. *Seismological Research Letters*, *70*, 59–80. https://doi.org/10.1785/gssrl.70.1.59

Stirling, M. W., Litchfield, N. J., Villamor, P., Van Dissen, R. J., Nicol, A., Pettinga, J., … Zinke, R. (2017). The M_w 7.8 2016 Kaikōura earthquake: Surface fault rupture and seismic hazard context. *Bulletin of the New Zealand Society for Earthquake Engineering*, *50*(2), 73–84.

Stirling, M. W., McVerry, G., Gerstenberger, M., Litchfield, N., Van Dissen, R., Berryman, K., … Jacobs, K. (2012). National seismic hazard model for New Zealand: 2010 update. *Bulletin of the Seismological Society of America*, *102*(4), 1514–1542. https://doi.org/10.1785/0120110170

Wallace, L. M., Kaneko, Y., Hreinsdottir, S., Hamling, I., Peng, Z., Bartlow, N., … Fry, B. (2017). Large-scale dynamic triggering of shallow slow slip enhanced by overlying sedimentary wedge. *Nature Geoscience*, *10*(10), 765–770. https://doi.org/10.1038/ngeo3021

Williams, C. A., Eberhart-Phillips, D., Bannister, S., Barker, D. H. N., Henrys, S., Reyners, M., & Sutherland, R. (2013). Revised interface geometry for the Hikuangi sub-duction zone, New Zealand. *Seismological Research Letters*, *84*, 1066–1073. https://doi.org/10.1785/0220130035

GRL

Supporting Information for

The 2016 Kaikōura earthquake revealed by kinematic source inversion and seismic wavefield simulations: Slow rupture propagation on a geometrically complex crustal fault network

C. Holden[1], Y. Kaneko[1], E. D'Anastasio[1], R. Benites[1], B. Fry[1] and I. J. Hamling[1]

[1]GNS Science, Lower Hutt, New Zealand

Contents of this file

Text S1 to S4
Figures S1 to S18
Tables Kaikoura_Source_ModelA.xlsx and Kaikoura_Source_ModelB.xlsx

Introduction

The supporting information contains detailed information on the forward modeling simulation technique including numerical discretization and rise time determination scheme (S1) and on quantitative description of the parameter range for the kinematic inversion (S2). S3 allows for quantitative comparison between waveform fits calculated from the forward simulation technique and those from the finite inversion method. S4 describes in detail the high-rate GPS data processing.

Figures S1 and S8 are cartoons of the Kekerengu fault in plane view (S1) as well as in cross section (S8). Figure S2 shows observed and synthetic velocity seismograms for a single-continuous rupture highlighting earlier phases not captured by this model. Figure S3 shows observed and synthetic displacement seismograms for isolated subduction rupture models. Figure S4 to S7 (respectively S10 to S13) show synthetic and observed velocity seismograms filter-band-passed 3—100 seconds for an extended set of regional stations and for both kinematic simulation models (respectively bandpass filtered 10-100 second). Figure S9 shows a comparison of coseismic displacements for different source models.

Figures S14 to S17 show synthetic and observed displacement seismograms bandpass filtered 3-60 seconds for an extended set of regional stations and for both kinematic simulation models.

Figure S18 illustrates kaik high-rate GPS station data recording of the Kaikōura earthquake.

Attached tables "Kaikoura_Source_ModelA.xlsx" and "Kaikoura_Source_ModelB.xlsx" provide detailed fault parameters for the two models proposed in the paper. These parameters are rupture time (s), risetime (s), latitude and longitude in degrees, depth (km), strike (degree), dip (degree), rake (degree), slip (m), patch length (m), patch width (m) and corresponding fault index.

Text S1.

Detailed forward wavefield simulation method

The computational region is 1200 km by 600 km at the Earth surface and extends to 400 km depth. This large computational domain has been set up to simulate earthquake ground motions across New Zealand (e.g., *Wallace et al., [2017]*). The mesh contains 4.7 million spectral elements; the average spacing between grid points at the Earth surface is 450 m. Minimum shear-wave velocity of Vs = 1.2 km/s is used in our simulations. The simulations use a time step of 0.010 s and are numerically accurate down to periods of about 2 s. To reduce the degree of unknowns, we use an *a-priori* fault slip model [*Clark et al., 2017*] as a constraint for the fault geometry and the final slip distribution, and only vary the rupture initiation times of major fault segments and rise time distribution (Figure 1a). The slip distribution in *Clark et al., [2017]* is constrained by high-resolution geodetic data (i.e., InSAR, GPS, and LiDAR) (Figure 1a; Figure S9) and surface mapping of uplift along the Kaikōura coast. In this slip model, there are a total of 21 planar fault segments with their dip constrained by geologically estimated values (Hamling et al., 2017). The surface trace of the faults is further constrained by discontinuities in the InSAR, including azimuth and range offsets, as well as LiDAR data. Each planar fault segment is discretized into 2 by 3 km patches along strike and dip, respectively, assuming constant dip. Most crustal faults that ruptured during the Kaikōura earthquake dip to the northwest.

Distributions of rupture initiation time and rise time are parameterized as follows. For simplicity, rupture velocity Vr is assumed to scale with the local 3D shear-wave velocity Vs such that Vr = Cr Vs., where the constant Cr is defined at individual fault planes. We vary a range of Cr, rupture initiation time, and its location on individual fault planes until the synthetic waveforms agree well with the observed ones. For many faults, the rupture initiation point in space is chosen at 10 km depth on the southwestern edge of individual faults. We select Cr, rupture initiation time and its location on individual fault planes to match the timing of main phases observed in waveforms at near-fault stations. Slip-rate evolution at each sub-fault is represented by a Gaussian function with half-duration. Following ground motion simulation approaches (e.g., *Aagaard et al., [2008]; Graves and Pitarka, [2010]*), we assume that local rise time Trise, which is equal to twice the half duration of the Gaussian source-time function, is proportional to the square root of slip and is given by Trise = Crise sqrt(slip), where slip is in meters and Trise in seconds. Wherever Trise becomes smaller than 3 s, we set Trise = 3 s. Since the minimum resolvable period for the computational mesh is ~2.5 s, we ensure well-resolved synthetic waveforms by setting the smallest Trise to be larger than the minimum resolvable period. Once an optimal rupture time distribution is found, constant Crise, assumed to be the same for all the fault planes, is also varied from 1.4 to 2.2 to fine-tune and improve waveform fits further; here we report the results with Crise = 1.6, which best-explain the observed waveforms at the selected frequency range of 0.01-0.333 Hz, chosen for reasons described in the main text.

We considered a total of 65 source models with the rupture velocity parameters Cr ranging from 0.4 to 0.9, the rise-time parameter Crise ranging from 1.4 to 2.2 $s/m^{1/2}$, and rupture initiation times ranging from 0 to 120 s. In the main text, we discuss the preferred model

that leads to the smallest waveform misfit and can explain main phases in nearfield velocity waveforms. By analyzing the waveform misfits for different source models, we find that the difference in the rupture velocity of more than 0.2 km/s is resolvable by the present technique and data.

We note that even with this relatively simple parameterization, there are a lot more free parameters than the total number of source models explored in this study due to computational limitation. As a result, the solutions are likely non-unique. This is why we compare features in the preferred source model with those derived from a more standard, kinematic source inversion approach described in section S2.

Text S2.

Quantitative description of the kinematic inversion parameters

We invert for an elliptical distribution of slip on each fault plane [Di Carli et al., 2010] described by nine parameters: the size (two semi-axis lengths) and location (along strike and along dip) of the ellipse, location of rupture starting time (along strike and along dip), rake, maximum slip, and rupture velocity. These vary for each individual fault plane but typical range of values for the largest fault planes are: size: 2-50 km and 2-50 km; location: 1-60 km and 1-50 km; rupture initiation location: 1-60km and 1-50 km; rake: 0-180degrees; maximum slip: 5-40 m; rupture velocity: 1-5 km/s.

We assume that the slip distribution D measured from the center of an ellipse has the Gaussian distribution $D(x,y) = Dm*\exp-(x^2/a^2+ y^2/b^2)$ where Dm is the maximum amplitude in the elliptical patch of semiaxes a and b. Geometries of the fault planes are fixed, but the rupture can originate anywhere on the fault plane.

In the case of the Kekerengu fault multiple inversion, we ran the inversion scheme three times, allowing for one elliptical slip patch each time, but adapting the time window to the phases of interest on the observed seismograms.

Text S3.

Waveform fit quantitative comparison

The waveform misfits of Model A, which are determined by calculating the sum of squared residuals for each step for all 17 stations, are 11.6 m^2/s^2, 17.6 m^2/s^2, and 6.0 m^2/s^2 for east-west, north-south and vertical components, respectively (Figures S4-S5). In calculating the misfit, both data and synthetic waveforms are 150 s long and re-sampled at a time step of 0.6 seconds. We also compare longer-period waveforms by bandpass filtering both data and synthetic seismograms between 10 and 100 s (Figure S10-S11), which result in smaller misfits.

The waveform misfits of Model B are 10.4 m^2/s^2, 15.1 m^2/s^2, and 16.6 m^2/s^2 for east-west, north-south and vertical components, respectively (Figures S6, S7). Longer-period waveforms obtained by band-pass filtering both data and synthetic seismograms between 10 and 100 s are shown on Figure S12 and S13.

Text S4.

High Rate GPS Data processing

10 Hz and 1 Hz high rate GPS data were retrieved from GeoNet (www.geonet.org.nz/) and LINZ (Land Information New Zealand, http://apps.linz.govt.nz/positionz/) continuous GPS sites. Epoch by epoch displacements in the North, East and Up components have been obtained with Track v. 1.29, the kinematic processing module of Gamit/Globk suite (Herring et al., 2016). IGS final orbits, ionospheric delay estimates, antenna phase center and differential code biases, have been used for the GPS data processing. *A priori* position of each site was taken from the 2016/11/12 daily positions obtained from daily solutions (http://www.geonet.org.nz/data/supplementary/gnss_time_series_notes). GPS station wark (Warkworth, a continuous GPS site ~600 km north of Kaikōura), has been used as reference site for the processing. Common displacement due to the surface wave arrival at WARK is ~300s after earthquake origin time, so its outside the time period of interest.

Interestingly, kaik GPS receiver temporarily lost tracking soon after the period of maximum shaking, between ~31 and ~32 sec after the earthquake origin time (Figure S18). This effect is quite infrequent, has been observed only a few times and is confirmed by some experiments performed by *Wang et al. [2012]* where they demonstrate large acceleration

and jerks can cause the receiver to stop tracking satellites. kaik was the only GPS site affected by this problem. That data gap has been taken into account into further analysis.
The high rate raw and rinex files are available onhttp://www.geonet.org.nz/data/supplementary/gnss_high_rate_data_access.

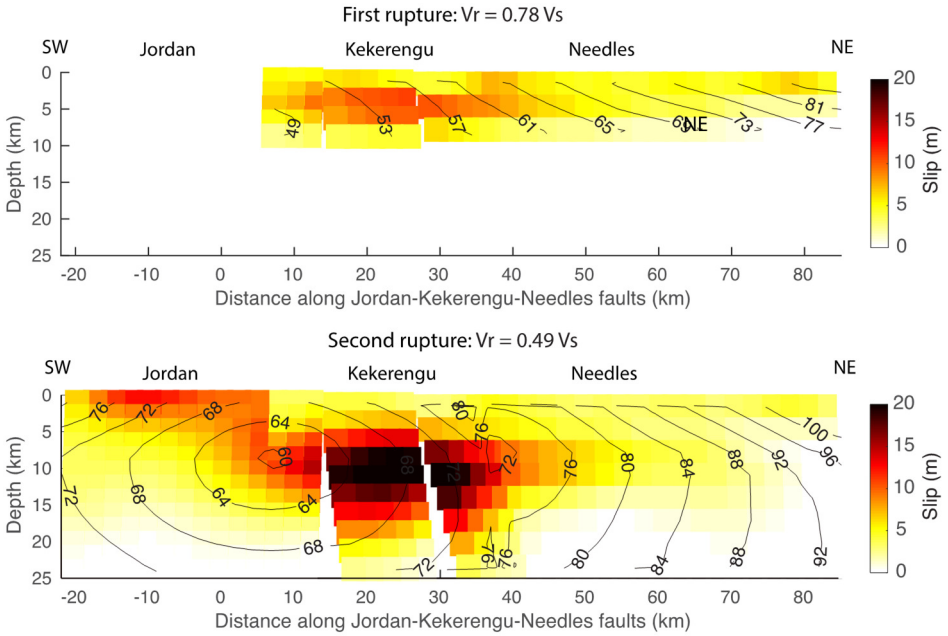

Figure S1. Slip distributions on the Jordan-Kekerengu-Needles faults in the source model derived from the wavefield simulation approach. The contours show rupture initiation times (time in seconds after the origin time).

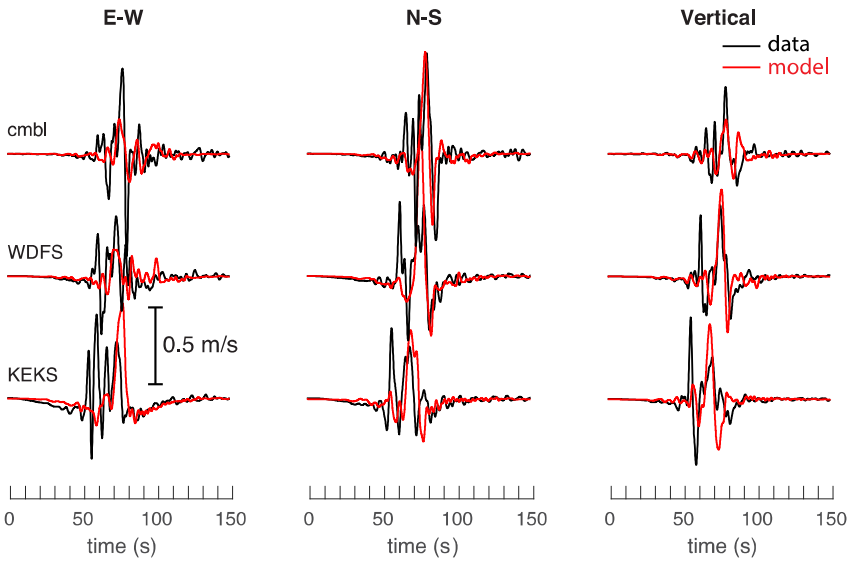

Figure S2. Observed (black line) and synthetic (red line) velocity seismograms bandpass filtered between 3 and 100 s at 3 northern near-fault stations for single-continuous rupture (Model A). The observed waveforms (black) show earlier phases (e.g., KEKS at time = 55 seconds) that are not captured by this model, indicating rupture re-reactivation on the Kekerengu fault.

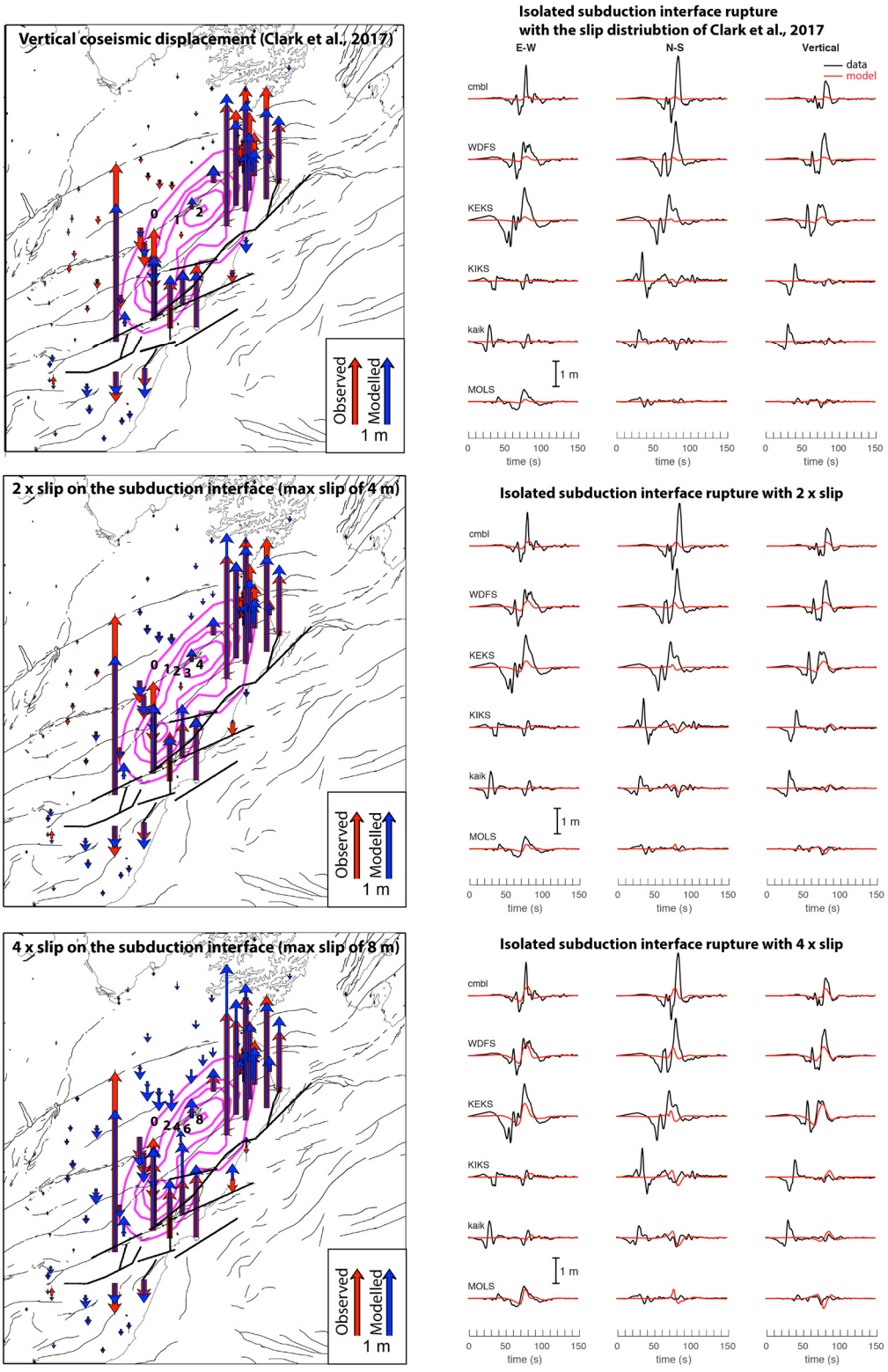

Figure S3. Observed (black line) and synthetic (red line) displacement seismograms bandpass filtered between 3 and 60 s at selected stations for isolated subduction interface rupture in Model A (Top), with twice larger slip (Middle) and 4 times larger slip (Bottom). The subduction interface slip constrained by geodetic observations (Clark et al., 2017) is unresolvable by the nearfield strong-motion waveforms (Top). As the amplitude of slip increases, the waveform amplitudes become larger and may be able to fit some of the phases (Bottom); however, the fit to vertcial geodetic data deteriorates (Bottom).

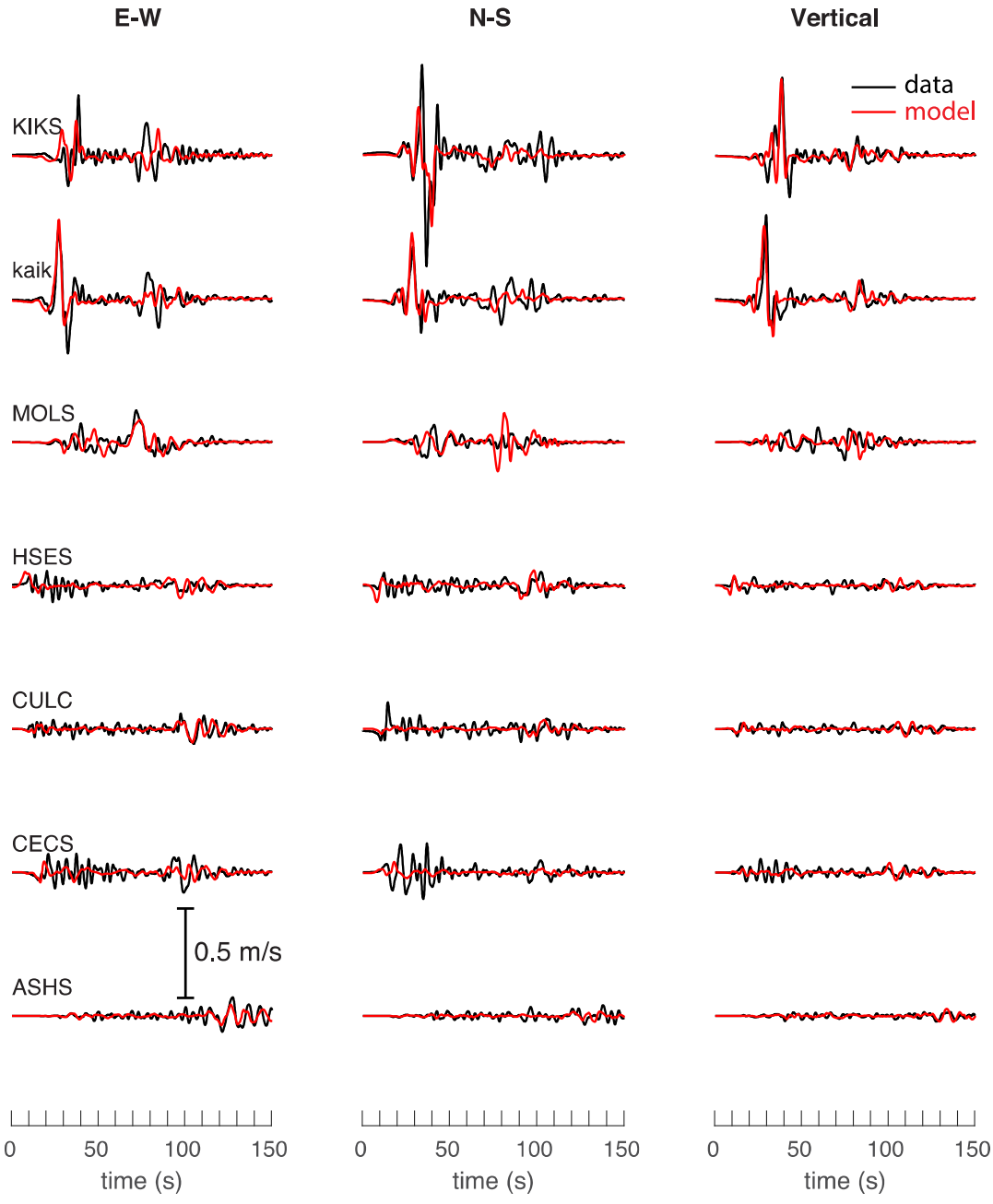

Figure S4. Observed (black line) and synthetic (red line) velocity seismograms bandpass filtered between 3 and 100 s at southern stations for the best-fit model (Model A). Note that high-rate GPS displacements at kaik in the time interval, 31.5 s < t < 32.2 s, are missing, likely due to a cycle slip on all satellites (Section S4). We applied cubic spline interpolation and covered the missing data over this relatively short time period.

Figure S5. Observed (black line) and synthetic (red line) velocity seismograms bandpass filtered between 3 and 100 s at northern stations for the best-fit (Model A). The model fits the onset polarities and amplitudes of dominant phases well.

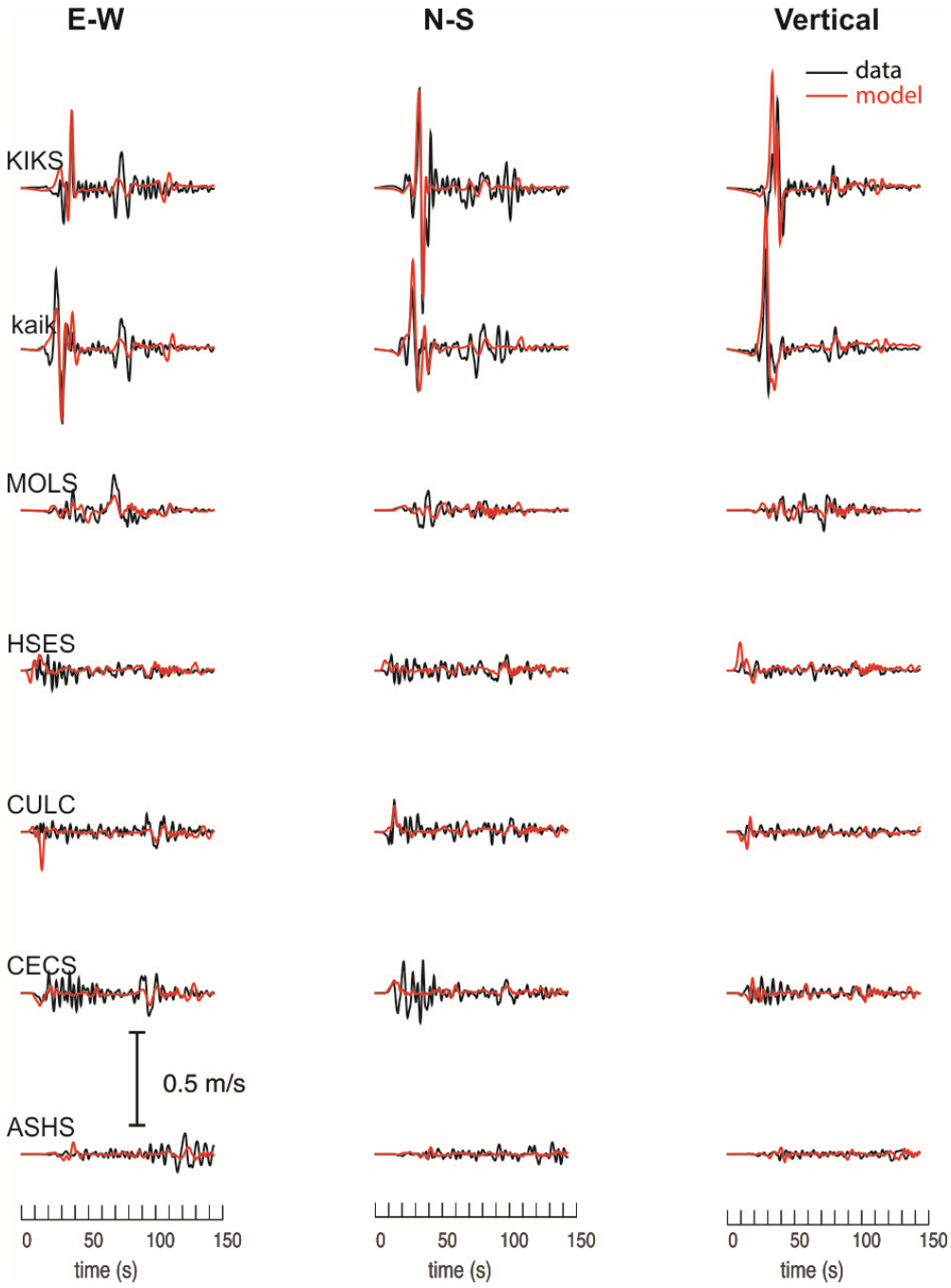

Figure S6. Observed (black line) and synthetic (red line) velocity seismograms bandpass filtered between 3 and 100 s (Model B); the duration is 150 seconds. The model fits the onset polarities and amplitudes well. (Stations located to the south). Note that high-rate GPS displacements at kaik in the time interval, 31.5 s < t < 32.2 s, are missing, likely due to a cycle slip on all satellites (Section S4). We applied cubic spline interpolation and covered the missing data over this relatively short time period.

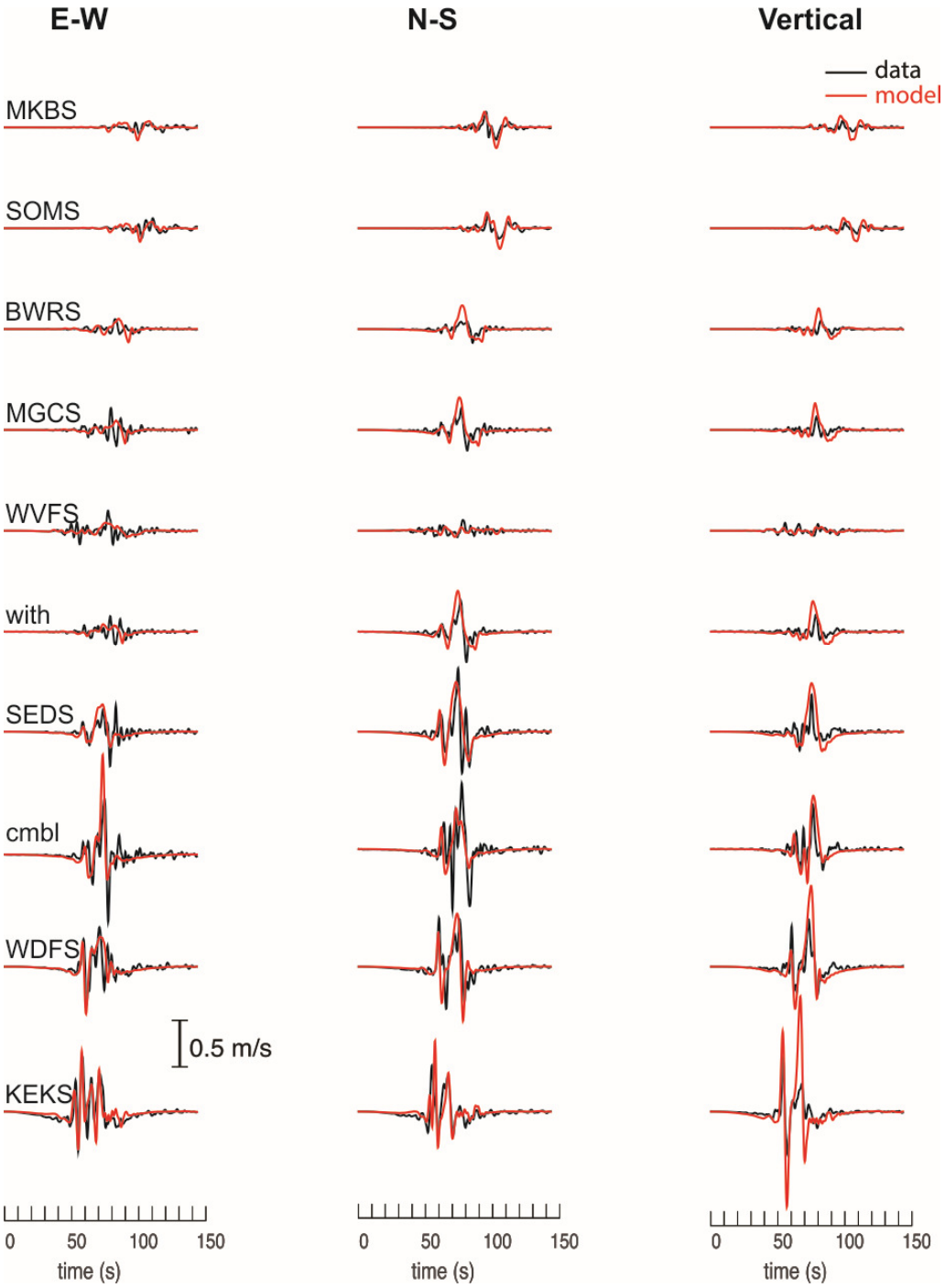

Figure S7. Observed (black line) and synthetic (red line) velocity seismograms bandpass filtered between 3 and 100 s (Model B); the duration is 150 seconds. Values above the traces are the maximum observed absolute velocities (m/s). The model fits the onset polarities and amplitudes well. (Stations located to the north).

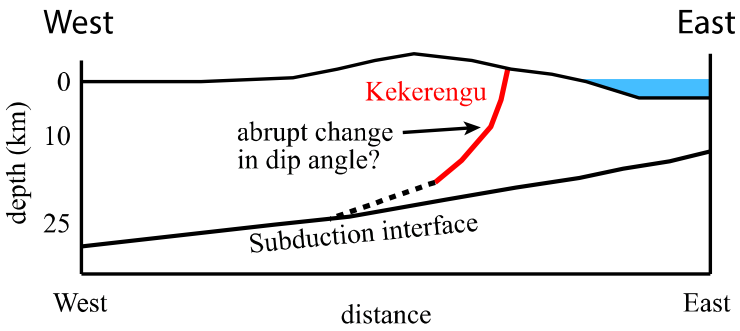

Figure S8. Cartoon illustrating a possible cause of rupture re-activation of the Kekerengu fault.

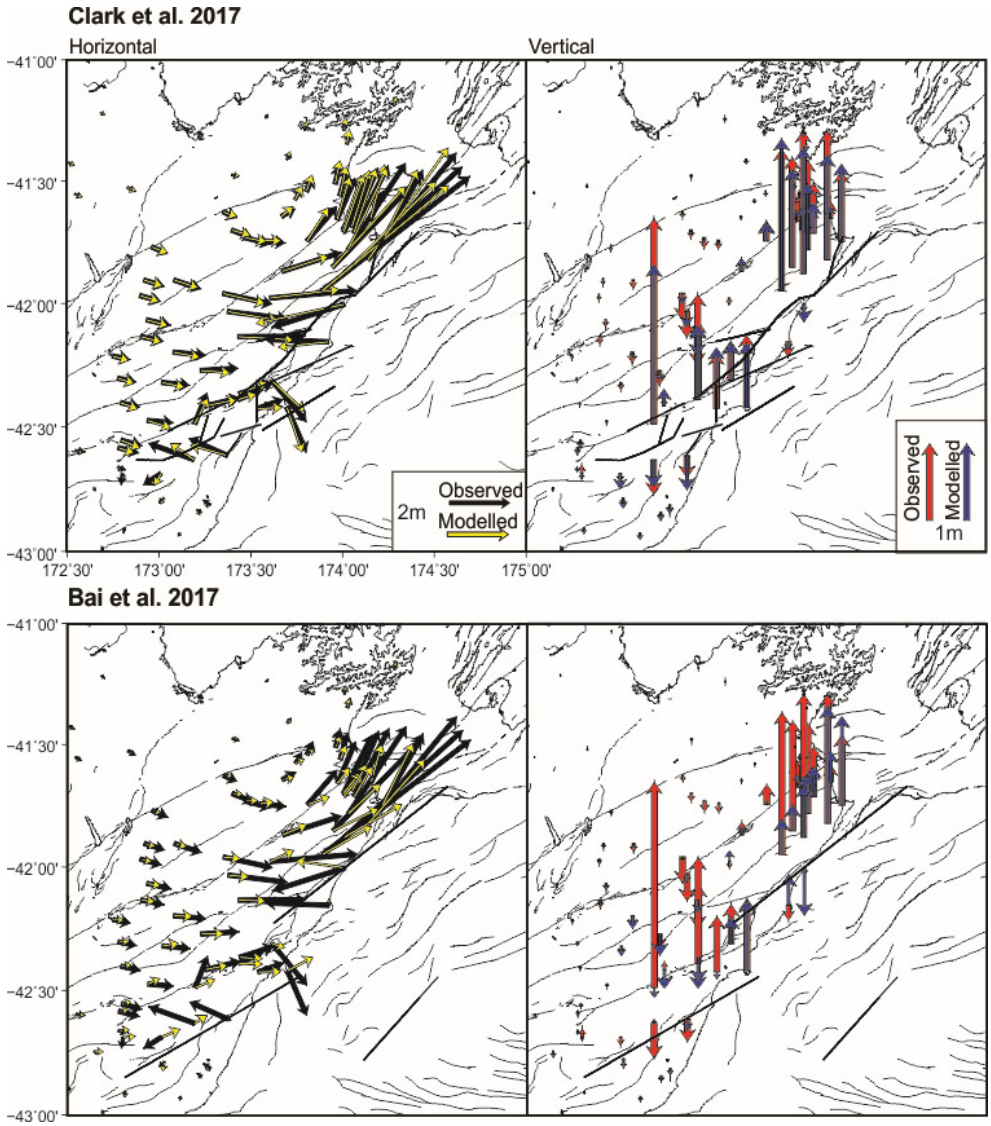

Figure S9. Comparison between coseismic displacement predicated by a slip model of Clark et al. (2017) (top) and Bai et al. (2017) (bottom) and GPS data shown in Hamling et al. (2017).

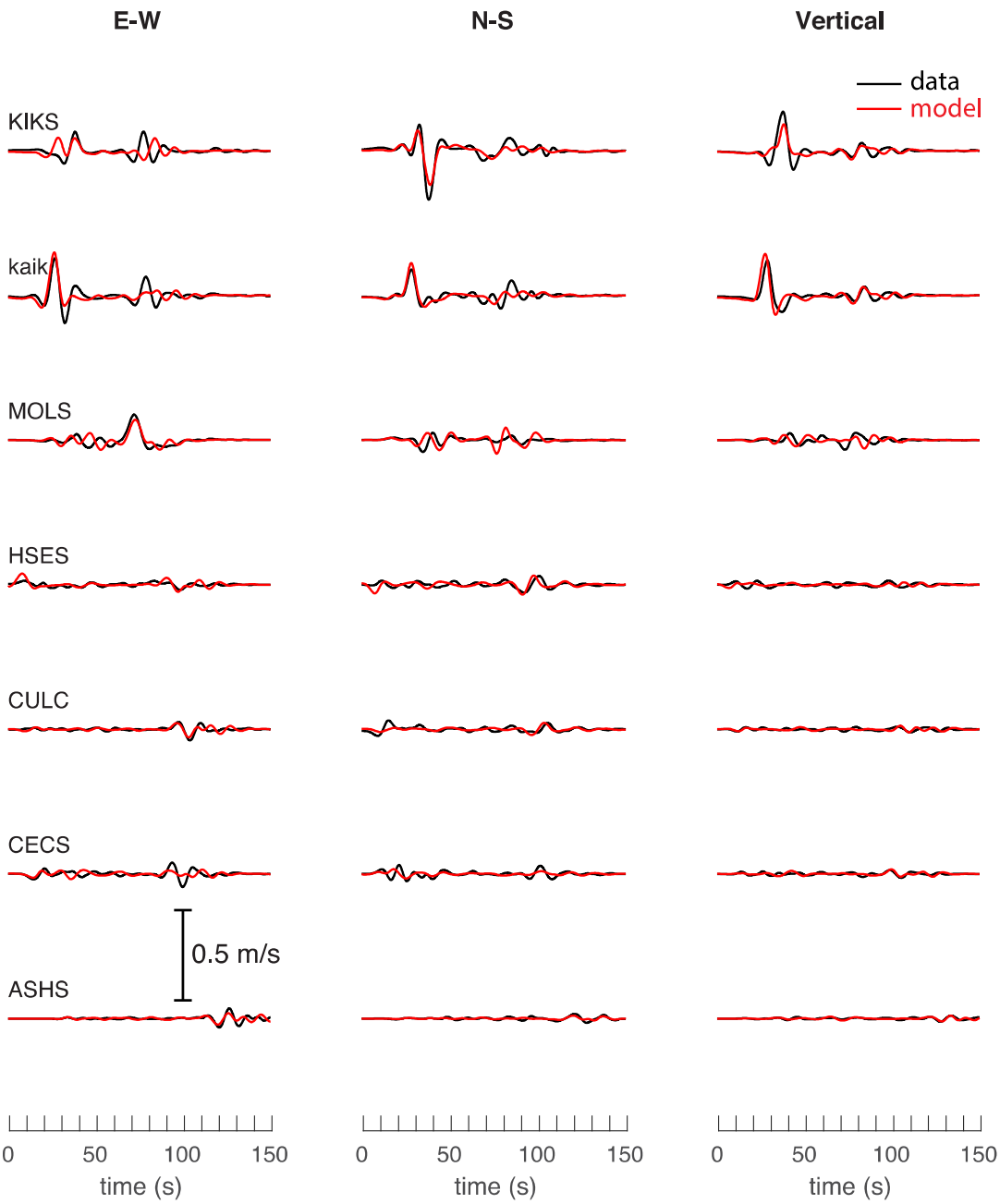

Figure S10. Observed (black line) and synthetic (red line) velocity seismograms bandpass filtered between 10 and 100 s at southern stations for the best-fit model (Model A). The model also fits the longer-period waves well.

Figure S11. Observed (black line) and synthetic (red line) velocity seismograms bandpass filtered between 10 and 100 s at northern stations (Model A). simulations. The model also fits the longer-period waves well.

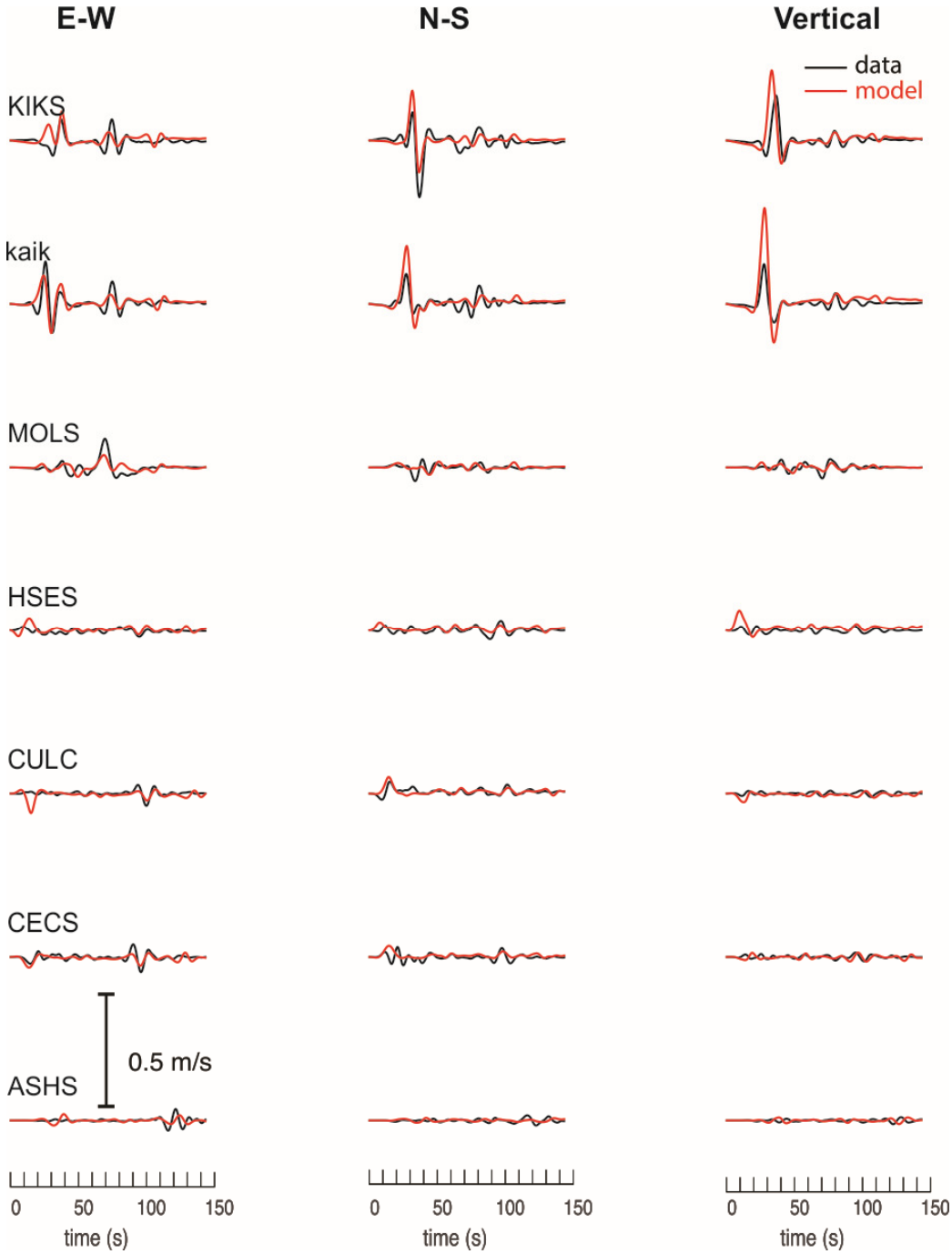

Figure S12. Observed (black line) and synthetic (red line) velocity seismograms bandpass-filtered at 10-100 seconds (Model B); the duration is 150 seconds. The model fits the onset polarities and amplitudes well. (Stations located to the south).

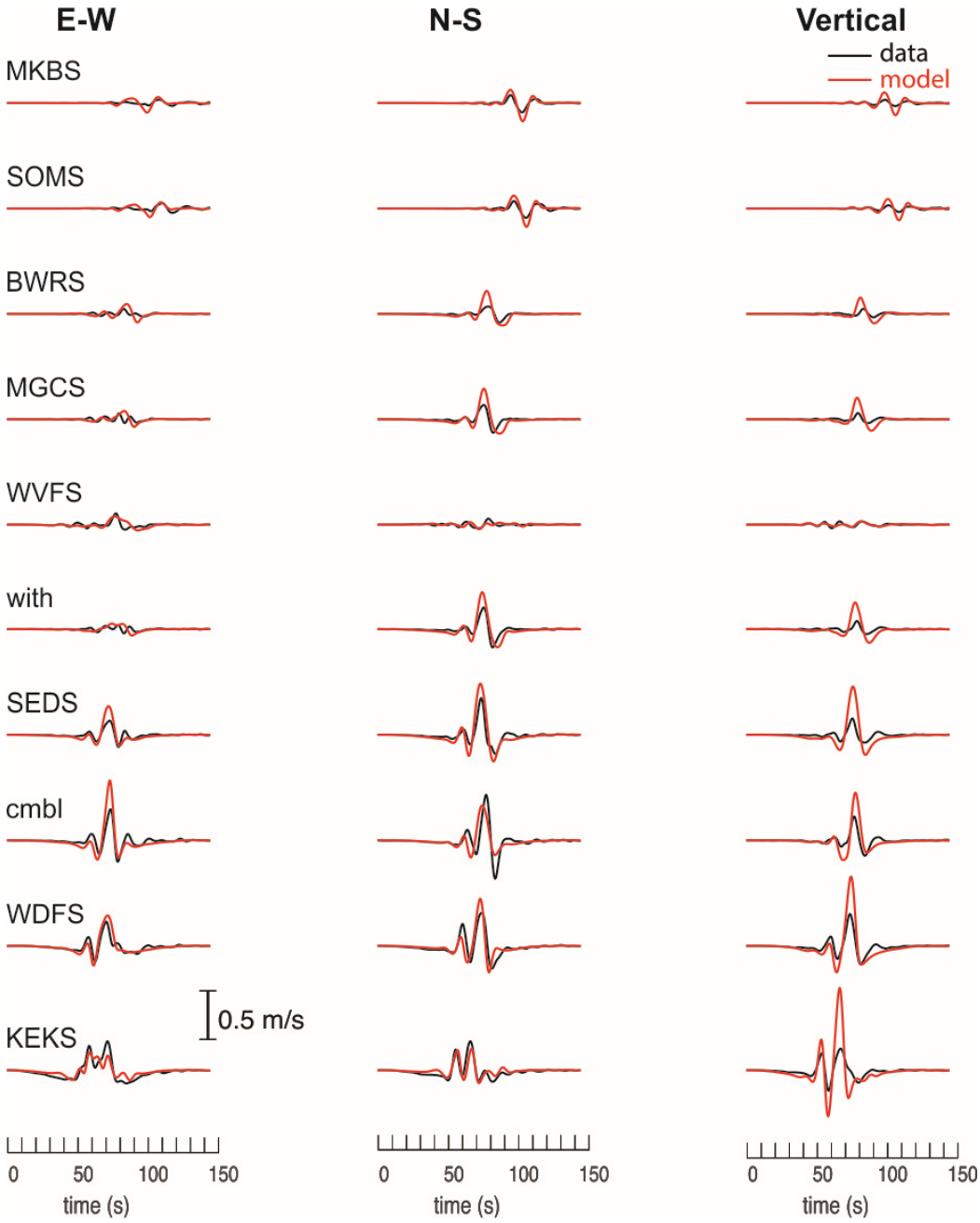

Figure S13. Observed (black line) and synthetic (red line) velocity seismograms bandpass filtered at 10 to 100 seconds (Model B); the duration is 150 seconds. The model fits the onset polarities and amplitudes well. (Stations located to the north).

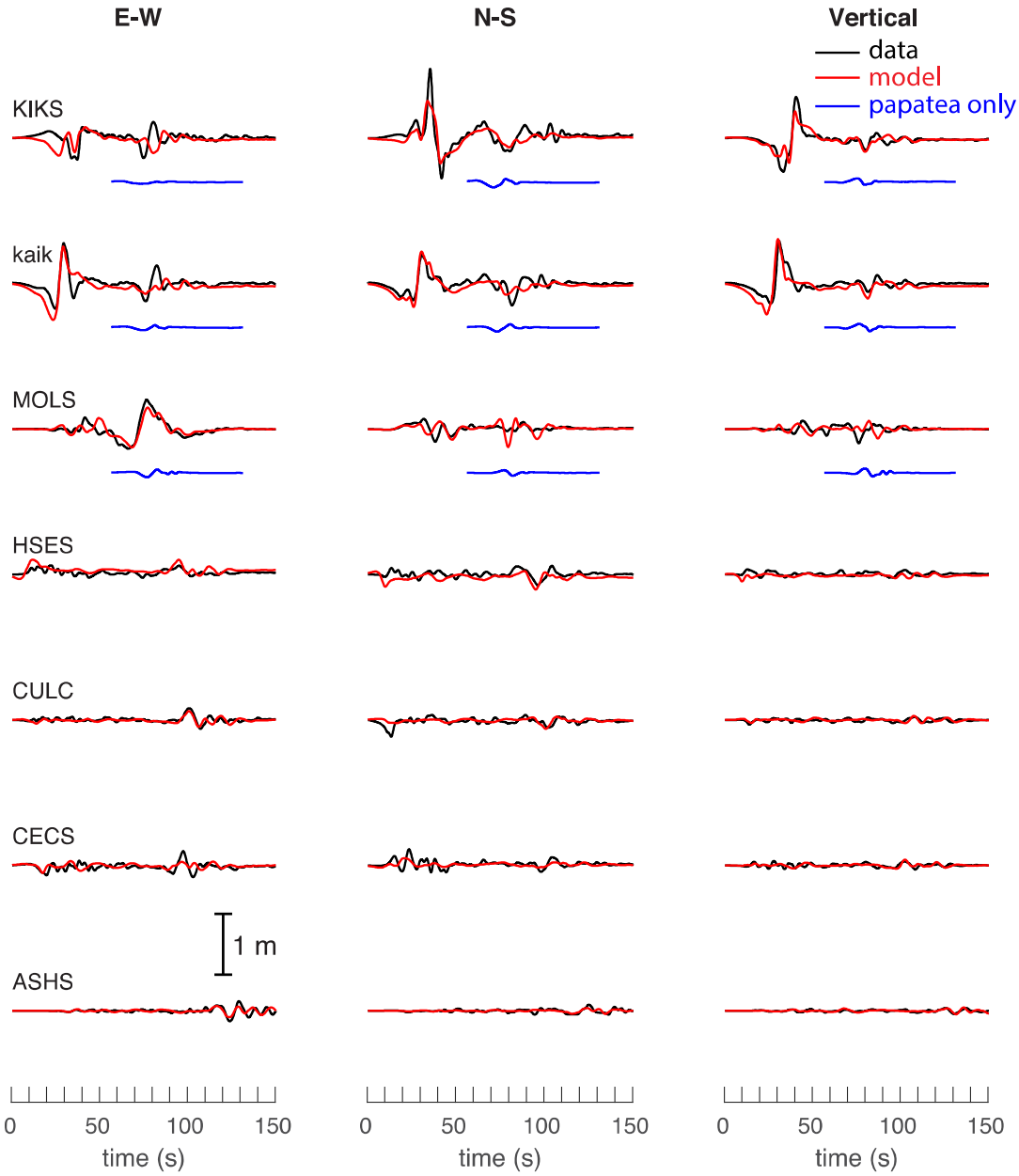

Figure S14. Observed (black line) and synthetic (red line) displacement seismograms bandpass filtered between 3 and 60 s at southern stations (Model A). simulations. The case with isolated rupture on a 13 km (width) by 15 km (depth) Papatea fault with uniform slip of 10 m and rupture velocity of ~1.5 km/s is also included in blue. Note that the Papatea fault only waveforms are smaller than waveforms due to the main asperity on the Kekerengu fault.

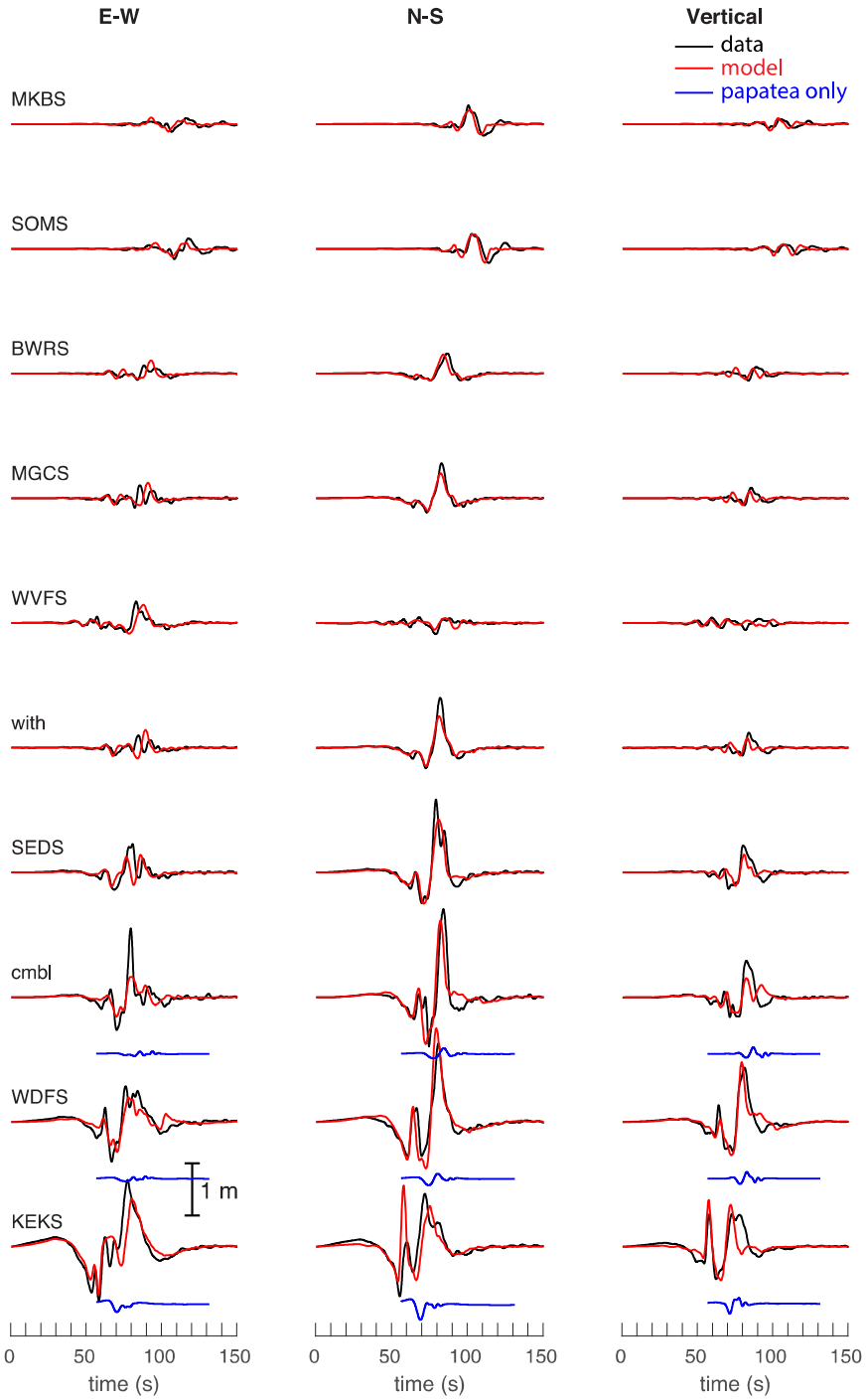

Figure S15. Observed (black line) and synthetic (red line) displacement seismograms bandpass filtered between 3 and 60 s at northern stations (Model A). The case with isolated rupture on a 13 km (width) by 15 km (depth) Papatea fault with uniform slip of 10 m and rupture velocity of ~1.5 km/s is also included in blue. Note that the Papatea fault only waveforms are smaller than waveforms due to the main asperity on the Kekerengu fault.

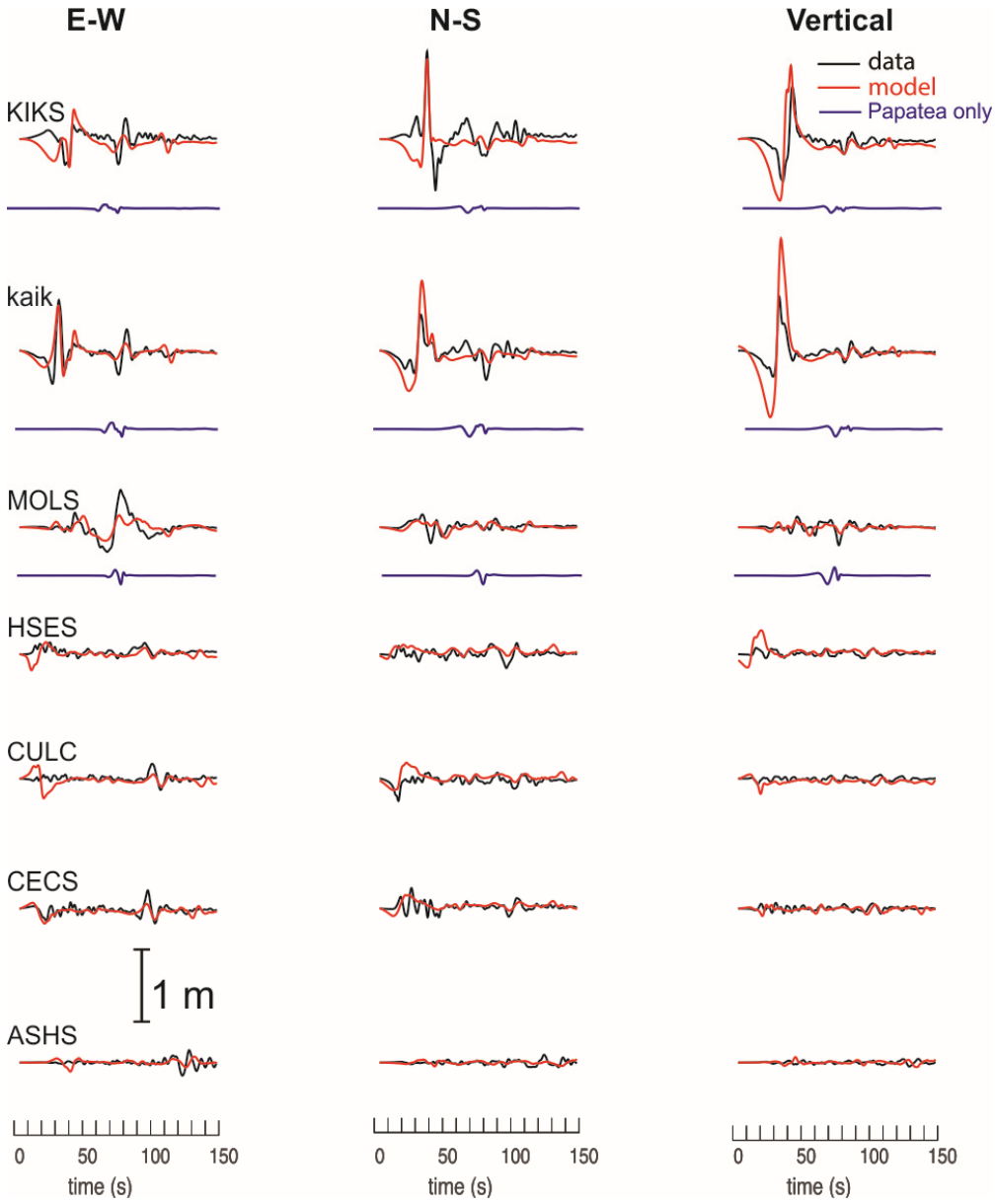

Figure *S16*. Observed (black line) and synthetic (red line) displacement seismograms bandpass filtered between 3 and 60 s at southern stations (Model B). The case with isolated rupture on a 13 km (width) by 15 km (depth) Papatea fault with uniform slip of 10 m and rupture velocity of ~1.5 km/s is also included in blue. Note that the Papatea fault only waveforms are smaller than waveforms due to the main asperity on the Kekerengu fault.

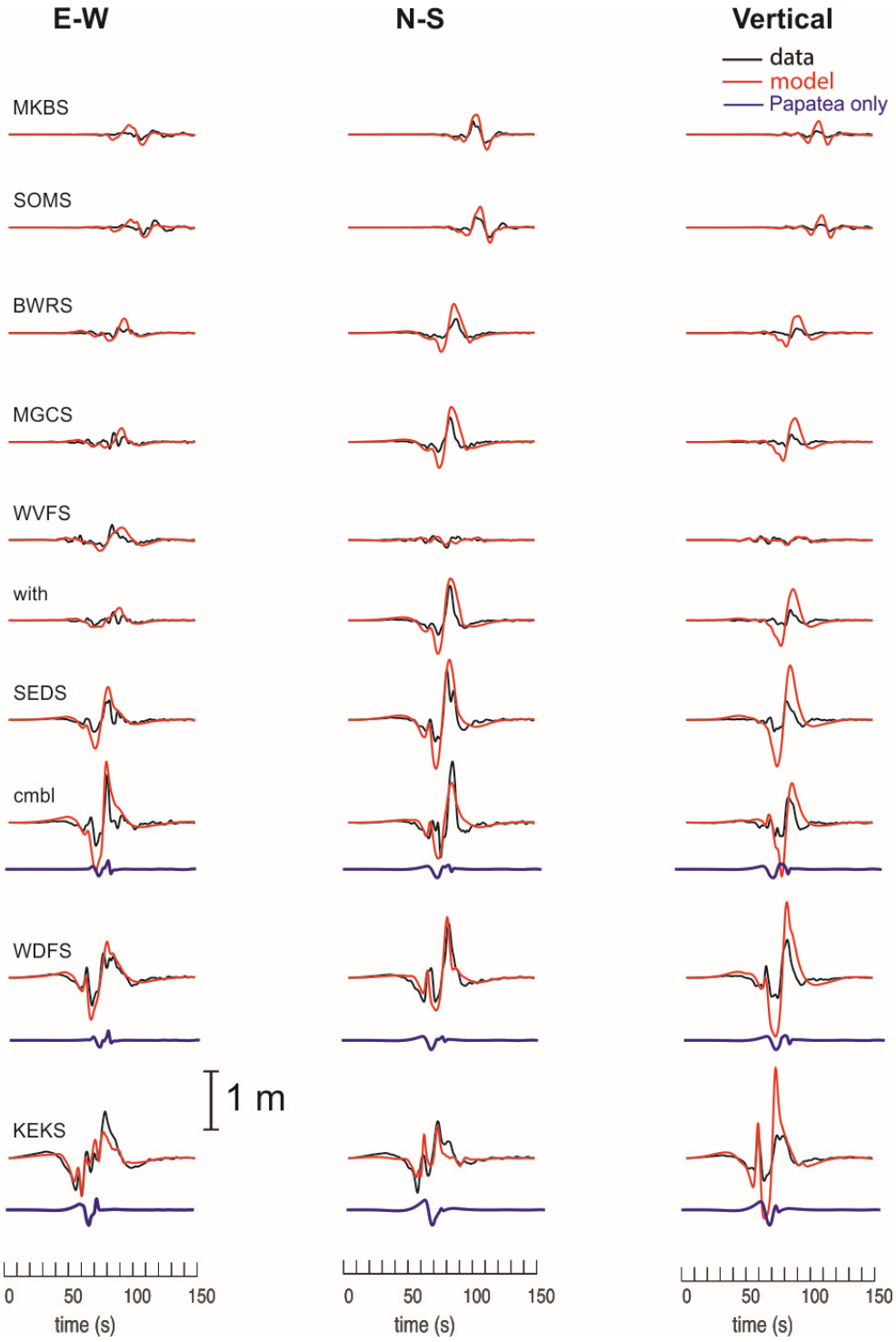

Figure S17. Observed (black line) and synthetic (red line) displacement seismograms bandpass filtered between 3 and 60 s at northern stations (Model B). The case with isolated rupture on a 13 km (width) by 15 km (depth) Papatea fault with uniform slip of 10 m and rupture velocity of ~1.5 km/s is also included in blue. Note that the Papatea fault only waveforms are smaller than waveforms due to the main asperity on the Kekerengu fault.

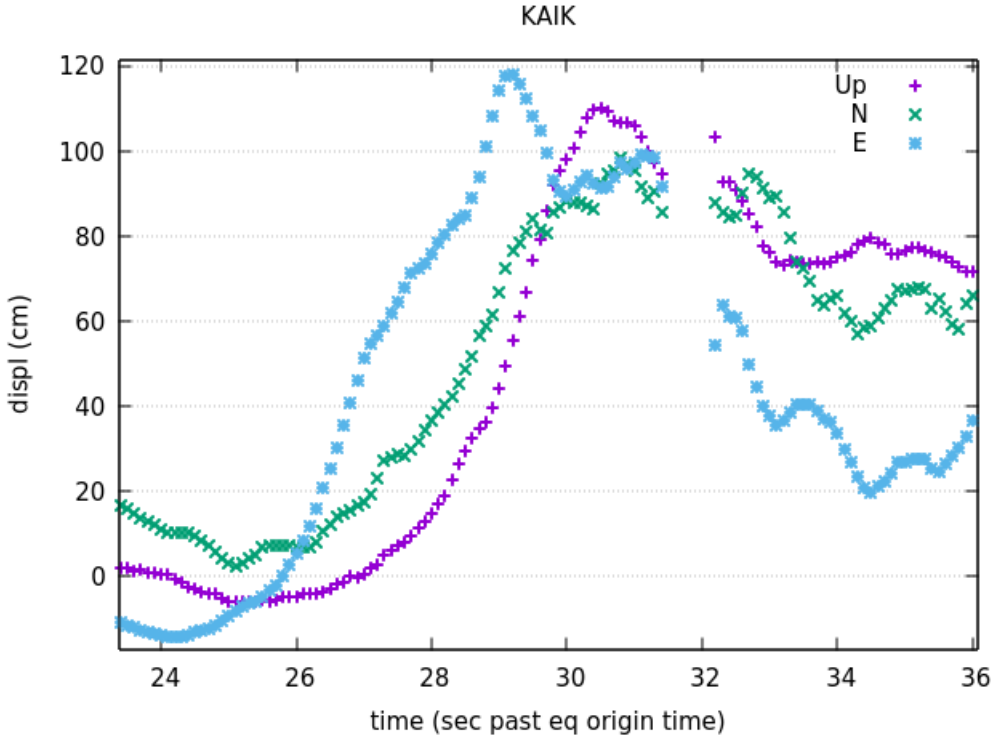

Figure S18. kaik high-rate GPS station data recording of the Kaikōura earthquake illustrating the GPS receiver temporarily losing tracking soon after the period of maximum shaking, between 31.5 and 32.1 sec after the earthquake origin time.